

---

# CMS Physics Analysis Summary

---

Contact: cms-pag-conveners-fsq@cern.ch

2013/07/27

## Measurement of Low $p_T$ Jet Cross Sections in proton-proton Collisions at $\sqrt{s} = 8$ TeV

The CMS Collaboration

### Abstract

We present a measurement of the inclusive jet cross section in proton-proton (pp) collisions at  $\sqrt{s} = 8$  TeV based on data collected by the CMS detector with an integrated luminosity of  $5.8 \text{ pb}^{-1}$ . The measurement was performed using the anti- $k_T$  clustering algorithm with a distance parameter  $R = 0.7$  in the rapidity region of  $|y| < 4.7$  for jet transverse momenta  $21 < p_T < 74 \text{ GeV}/c$ . The measured jet cross-section is compared to predictions of next-to-leading order (NLO) QCD calculations.



# 1 Introduction

Events with high transverse momentum jets in proton-proton collisions are described by quantum chromodynamics (QCD) in terms of parton-parton scattering, where the outgoing scattered partons manifest themselves as hadronic jets. In this frame the partonic cross section is convoluted with the parton density functions (PDF), which give the probability to find a parton with a momentum fraction  $x$  of the protons momentum at a resolution scale  $\mu$ . The factorisation of the cross section into a perturbatively calculable partonic part and the parton density functions is a fundamental property of the theory.

A measurement of the jet cross section as a function of the rapidity  $y$  and the transverse momentum  $p_T$  of the jet is a sensitive probe for the calculation of the hard partonic cross section as well as for the parton densities. The rapidity is defined as  $y = \frac{1}{2} \ln \frac{E+p_z}{E-p_z}$ , with  $E, (p_z)$  being the energy, (longitudinal momentum component) of the jet, respectively.

The measured inclusive jet cross section at  $\sqrt{s} = 7$  TeV [1–3] is in reasonable agreement with theoretical calculations at next-to-leading order (NLO) in the strong coupling  $\alpha_s$  at small  $y$ , while differences are observed at large  $y$ . Especially of interest is the region of small  $p_T$  and large  $y$  because partons with a small momentum fraction  $x$  are involved, where the parton density, especially the gluon density becomes large. In addition, in the region of small  $x$ , new effects might show up, when the transverse momentum of the interacting partons cannot be neglected and a different parton evolution scheme might be more appropriate [4–6].

Jets are measured in events recorded at  $\sqrt{s} = 8$  TeV with the anti- $k_T$  algorithm [7] in the ranges  $|y| < 4.7$  and  $p_T = 21 - 74$  GeV/c. The measured jets are corrected to hadron level and the resulting cross sections are compared to theoretical predictions at NLO QCD with NLOJET++ [8, 9] using different PDFs.

The paper is organised as follows. Sections 2 and 3 describe respectively the experimental apparatus and the data sample used in the analysis. The jet reconstruction and jet energy corrections are presented in Sections 4 and 5 respectively. The experimental results and associated uncertainties discussed in Section 6 are compared to the theoretical predictions in Section 7. The main conclusions of the study are summarised in Section 9.

## 2 Experimental setup

The CMS detector is described in detail elsewhere [10]. The central part of the CMS detector is a superconducting solenoid, which provides an axial magnetic field of 3.8 T parallel to the beam axis. Charged particle trajectories are measured by the silicon pixel and strip tracker, which cover the pseudorapidity region  $|\eta| < 2.5$ . A crystal electromagnetic calorimeter (ECAL) and a brass/scintillator hadron calorimeter (HCAL) surround the tracking volume and cover  $|\eta| < 3.0$ . A quartz-fibre Cherenkov calorimeter (HF) extends the coverage to  $|\eta| = 5.2$ . Muons are measured in gas detectors embedded in the iron return yoke outside the solenoid, in the pseudorapidity range  $|\eta| < 2.5$ .

The most important components relevant for the jet reconstruction analysis are the ECAL and HCAL central calorimeters [11, 12], as well as the HF forward calorimeters [13]. The ECAL calorimeter cells are grouped in projective towers of granularity in pseudorapidity and azimuthal angle of  $\Delta\eta \times \Delta\phi = 0.0174$  (barrel) – 0.05 (endcap). The relative transverse energy resolution of ECAL is about  $3\%/\sqrt{E_T[\text{GeV}]}$  for electromagnetic particles. The HCAL has a tower granularity of  $\Delta\eta \times \Delta\phi = 0.087$  and a transverse energy resolution of about  $100\%/\sqrt{E_T[\text{GeV}]}$  for hadrons. The HF calorimeters consist of iron absorbers with embedded radiation-hard quartz

fibres, located at 11.2 m from the interaction point on both sides of the experiment covering the region of  $2.9 < |\eta| < 5.2$ . Half of the HF fibres run over the full depth of the absorber, while the other half start at a depth of 22 cm from the front of the detector. The  $\eta$ - $\phi$  tower segmentation of the HF calorimeters is  $0.175 \times 0.175$ , except for  $|\eta|$  above 4.7 where the segmentation is  $0.175 \times 0.35$ . The HF total energy resolution is of about  $200\%/\sqrt{E[\text{GeV}]}$ .

### 3 Data sample and event selection

In this analysis the data collected during 2012 with low pile-up runs with an average of 4 interactions per bunch crossing by the CMS experiment at the centre-of-mass energy of 8 TeV are used. The data sample used for the jet cross section measurements corresponds to  $5.8 \text{ pb}^{-1}$  of integrated luminosity.

Events for the inclusive jet analysis were collected with a Zero Bias trigger which requires at least two charged tracks reconstructed in the pixel detector, in coincidence with the correct bunch crossing. The selected events were required to have a good primary vertex (PV) consistent with the measured transverse position of the beam: the PV was required to be reconstructed from at least 5 tracks and to lie within  $\pm 24$  cm in the longitudinal direction with respect to the nominal interaction point. This selection is highly efficient ( $\approx 100\%$ ) for this analysis and rejects non-collision background.

### 4 Jet reconstruction

The infrared and collinear safe anti- $k_T$  jet clustering algorithm [14] is used to reconstruct jets with a distance parameter of  $R = 0.7$ . The clustering is performed by four-momentum summation where the chosen size parameter allows for the capture of most of the parton shower. The inputs to the jet clustering algorithm are the four-momentum vectors of particle-flow (PF) objects. Individual particles (leptons, photons, charged and neutral hadrons) are reconstructed with the particle-flow technique [15] which combines the information from several sub-detectors. PF objects are reconstructed in different CMS regions: In the central region tracker, HCAL, ECAL and muon system are used while in the forward region only HF information is available. For example, electrons are reconstructed from tracks and calibrated ECAL clusters; muons are reconstructed using tracks; charged hadrons are reconstructed from tracks and calibrated ECAL and HCAL clusters; photons and neutral hadrons are reconstructed from calibrated ECAL and HCAL clusters, respectively.

### 5 Jet energy corrections

The raw jet  $p_T$  spectra need to be corrected to account for various experimental effects. The reconstructed jet energy is first absolutely calibrated with correction factors derived using real data, via a  $p_T$ -balancing method in dijet and in photon-jet events, as well as from MC simulations [16, 17]. The applied jet energy corrections account for the relative  $\eta$  and  $p_T$  dependence of the response of the ECAL, HCAL and HF calorimeters, and restore the absolute jet energy scale (JES) to the calibrated values. The correction also removes extra energy from pp pile-up events.

The jet energy correction (JEC) depends on the  $\eta$  and  $p_T$  of the jet, and is applied as a multiplicative factor to the jet four-momentum vector. The multiplicative factor is in general smaller than 1.2, and approximately uniform in  $\eta$ .

## 6 Inclusive jet cross sections

The measured differential inclusive jet cross section is defined by the basic formula

$$\frac{d^2\sigma}{dp_T dy} = \frac{1}{\mathcal{L}_{\text{eff}}} \cdot \frac{N}{\Delta p_T \cdot \Delta y} \quad [\text{pb}/(\text{GeV}/c)] \quad (1)$$

where  $N$  is the number of jets in the bin,  $\Delta p_T$  and  $\Delta y$  are the bin widths in  $p_T$  and  $y$ , respectively.  $\mathcal{L}_{\text{eff}}$  is the effective integrated luminosity of the corresponding data sample from which the events are taken. The width of the  $p_T$  bins is progressively increased with  $p_T$ , proportional to the  $p_T$  resolution. The phase space in rapidity  $y$  is subdivided into six equally sized regions of absolute rapidity from  $|y| = 0$  up to  $|y| = 3$  with  $\Delta|y| = 0.5$ . Hence, the bin width in  $y$  is  $\Delta y = 1$ . In the forward region ( $3.2 < |y| < 4.7$ ),  $\Delta|y| = 1.5$  and the bin width in  $y$  is  $\Delta y = 3$ . The measured spectra are then corrected for detector smearing effects (unfolded to the particle level), using the iterative (d'Agostini) method [18], as implemented in the RooUnfold package [19].

The primary sources of systematic uncertainty in the jet cross sections measurements are taken into account:

- There is an asymmetric systematic uncertainty on the measured cross section due to Jet Energy Scale (JES) [20], which is the dominant source of systematic uncertainty for jet cross sections. The JES uncertainty is dependent on  $p_T$  and  $\eta$  and has been estimated to be 2 – 6% at  $|y| < 4.7$  and it gives rise to 5% to  $\approx 45\%$  uncertainty on the final jet cross section. The individual, uncorrelated contributions to the JES uncertainty have been estimated. The JES uncertainty sources account for the  $p_T$  and  $\eta$  dependence of the JES within the total uncertainty. For this analysis, 16 mutually uncorrelated sources contribute to the total JES uncertainty. The uncertainty sources are divided into four broad categories: pile-up effects, relative calibration of jet energy scale versus  $\eta$ , absolute energy scale including  $p_T$  dependence, and differences in quark - and gluon-initiated jets [3].

**Pile-up effects:** The pile-up uncertainties include data/MC difference from the data-based Random Cone method run on Zero Bias data, variation in the amount of out-of-time pile-up in various samples and data-taking eras, and the dependence of jet rates (i.e. jet cross section) on the average number of primary vertices per run  $\langle N_{PV} \rangle$ . Pile-up uncertainties also include systematics from offset dependence on jet  $p_T$  and data-based method bias.

**$\eta$ -dependent effects:** These effects parameterize the possible relative variations in JES, which for the dijet and inclusive jet analyses lead to correlations between rapidity bins. In principle these effects could also have a  $p_T$  dependence, but systematic studies on data and MC events indicate that the  $p_T$  and  $\eta$  dependence of the uncertainties factorize to a good approximation.

**Absolute energy scale and its  $p_T$  dependence:** The  $p_T$  dependent uncertainty arising from modeling of the underlying event and jet fragmentation is obtained by comparing predictions from PYTHIA 6 [21] and HERWIG ++ [22].

The final uncertainty arises from differences in the JES for quark and gluon-initiated jets and is determined from MC studies.

- The uncertainty on the integrated luminosity is estimated to be 4.4% which propagates directly to the measurement of cross section.

- The unfolding uncertainty introduces a 3% to 25% uncertainty on the cross section measurement.
- Jet Energy Resolution propagates to 3% – 17% uncertainty on the measurement.

## 7 Theoretical predictions

The theoretical predictions for the jet cross sections consist of next-to-leading order QCD calculation and a non-perturbative correction to account for multiparton interactions (MPI) and hadronisation effects. In previous analyses [2, 23–25] the non-perturbative correction was derived from the average predictions of two LO Shower Monte Carlo (SMC) event generators PYTHIA and HERWIG ++. In the present analysis, an alternative method is used, which uses the NLO MC event generator POWHEG [26, 27] for the hard subprocess complemented with the hadronisation and showering from the SMC program.

The NLO calculations are done using the NLOJet++ program (v2.0.1) [28] within the framework of the fastNLO package (v1.4) [29]. The renormalization and factorization scales ( $\mu_R$  and  $\mu_F$ ) for the inclusive measurement, are equal to the jet  $p_T$ . The NLO calculation is performed using five different PDF sets: CT10 [30], MSTW2008NLO [31], NNPDF2.1 [32], HERAPDF1.5 [33], and ABM11 [34] at the corresponding default values of the strong coupling constant  $\alpha_S(M_Z) = 0.118, 0.120, 0.119, 0.1176$ , and  $0.1179$  respectively. In order to compare NLO theory calculation with corrected data, the parton-level calculations have to be corrected for various effects.

The NLO parton level calculation has to be supplemented with corrections due to non-perturbative effects (hadronisation and multiparton interactions) as well as effects coming from parton showers in the initial and final state. Both corrections have been estimated with POWHEG according to the method described in Ref. [35]

The variation of  $\alpha_S(M_Z)$  by 0.001 introduces 1–2% uncertainty on the theoretical prediction. The renormalization and factorization scale uncertainty is estimated as the maximum deviation at the six points  $(\mu_F/\mu, \mu_R/\mu) = (0.5, 0.5), (2, 2), (1, 0.5), (1, 2), (0.5, 1), (2, 1)$ , where  $\mu = p_T$  (inclusive). An additional uncertainty up to 13% is caused by the non-perturbative and parton showers corrections. Hence, the total theoretical uncertainty reach up to 14%.

## 8 Results

The inclusive jet cross section corrected to hadron level as a function of  $p_T$  for different bins in rapidity  $y$  is shown in Fig. 1. The cross section is steeply falling with increasing  $p_T$ . The slope of the  $p_T$  distribution becomes steeper with increasing rapidity  $y$ . Tables 1 - 3 tabulate the  $p_T$  differential cross sections corrected to hadron level and their associated uncertainties. In Fig. 2 to Fig. 6 the ratio of the measurement to the theoretical predictions using different PDF sets is shown. The experimental and theoretical systematic uncertainties are shown. The total experimental uncertainty band is dominated by the JES uncertainty. Together with the uncertainty from the JER, unfolding and luminosity, can reach 60% especially in the low  $p_T$  region. The total theoretical uncertainty, obtained by adding quadratically the uncertainties from NP and PS corrections and the scales can reach 14%. Within the uncertainties, the measurements agree reasonably well with all predictions. A similar comparison but instead of the theoretical uncertainty for each PDF set the ratios of the predictions with alternative PDF sets is shown in Fig. 7 - 11.

Although the experimental uncertainties are in some regions larger than the theoretical uncertainties, these measurements can provide significant constraints to the theoretical calculations. Applying correction factors to account for higher order parton radiation (parton shower correction) brings the parton level calculations in agreement with the measurements: the cross sections are well described over the full  $p_T$  and  $y$  range. With this agreement, the measured jet cross sections can be used in global fits to further constrain the proton parton density distributions.

## 9 Summary

The  $p_T$ -differential cross sections for the inclusive production of jets in the rapidity ranges  $|y| < 4.7$  has been measured by the CMS detector using  $5.8 \text{ pb}^{-1}$  of low pile-up data collected in proton-proton collisions at  $\sqrt{s} = 8 \text{ TeV}$ . Jets were reconstructed using the anti- $k_T$  algorithm ( $R = 0.7$ ) in the  $p_T$  range of  $21 - 74 \text{ GeV}/c$ . The results have been shown in terms of differential inclusive jet cross sections for seven rapidity bins. Detailed studies of various experimental and theoretical uncertainties, and their relative comparison are carried out. The dominant source of systematic uncertainty arises due to the JES which propagates about  $5 - 45\%$  uncertainty on the cross section measurement across varying rapidity bins. The measured differential jet cross section is compared with the  $\text{NLO} \times \text{NP} \times \text{PS}$  theory predictions based on perturbative QCD predictions corresponding to five different PDF sets. Within the current experimental and theoretical uncertainties, perturbative QCD calculations are in agreement with the measured inclusive jet cross sections.

The ratio of the data to the theoretical predictions is shown for the five PDF sets in Fig. 13 - Fig. 17. The values of ratio are obtained from the present low- $p_T$  ( $21 < p_T < 74 \text{ GeV}/c$ ) and high- $p_T$  jet ( $p_T > 74 \text{ GeV}$ ) [25] measurements.

## Acknowledgments

We thank the technical and administrative staff at CERN and other CMS Institutes, and acknowledge support from: FMSR (Austria); FNRS and FWO (Belgium); CNPq, CAPES, FAPERJ and FAPESP (Brazil); MES (Bulgaria); CERN; CAS, MST and NSFC (China); MST (Croatia); RPF (Cyprus); Academy of Sciences and NICPB (Estonia); Academy of Finland, ME and HIP (Finland); CEA and CNRS/IN2P3 (France); BMBF, DFG and HGF (Germany); GSRT and Leventis Foundation (Greece); OTKA and NKTH (Hungary); DAE and DST (India); IPM (Iran); SFI (Ireland); INFN (Italy); KICOS (Korea); CINVESTAV, CONACYT, SEP and UASLP-FAI (Mexico); PAEC (Pakistan); SCSR (Poland); FCT (Portugal); JINR (Armenia, Belarus, Georgia, Ukraine, Uzbekistan); MST and MAE (Russia); MSD (Serbia); MCINN and CPAN (Spain); Swiss Funding Agencies (Switzerland); NSC (Taipei); TUBITAK and TAEK (Turkey); STFC (United Kingdom); DOE and NSF (USA).

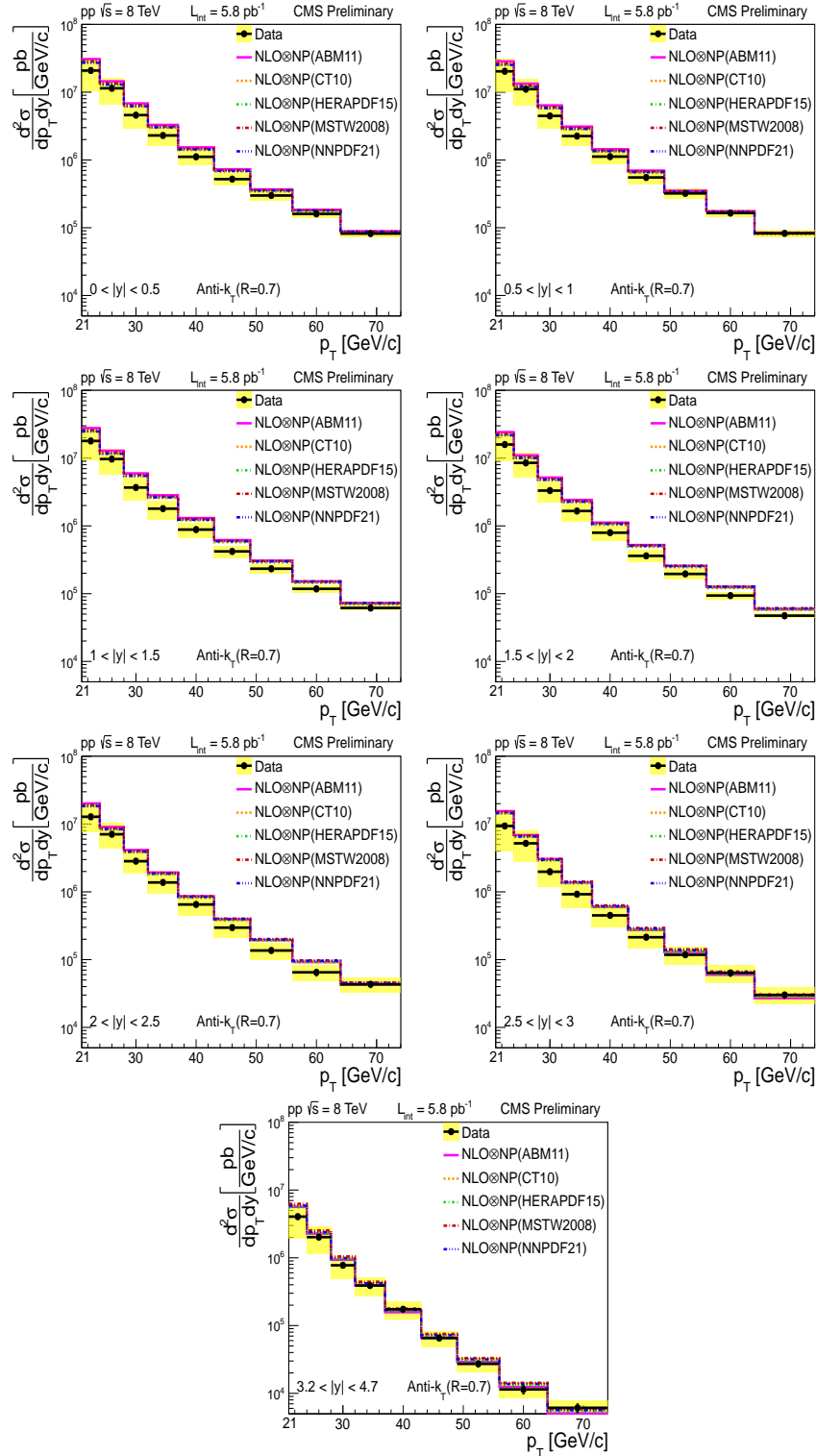


Figure 1: Inclusive jet cross section (anti- $k_T$ ,  $R = 0.7$ ) measured at rapidities ( $|y| < 4.7$ ) as a function of transverse momentum, fully corrected and unfolded, compared to various hadron-level theoretical predictions: NLO calculations for various PDFs. The yellow band on the data points refers to the total experimental uncertainty.



Table 1: The  $p_T$  differential cross section corrected to hadron level for inclusive jets at  $0 < |y| < 0.5$  and  $0.5 < |y| < 1$ . The first (second) uncertainty reflects the statistical (systematic) contribution.

$p_T$ [GeV/c]	$\frac{d^2\sigma}{dp_T dy}$ [pb/(GeV/c)] $0 <  y  < 0.5$	$\frac{d^2\sigma}{dp_T dy}$ [pb/(GeV/c)] $0.5 <  y  < 1$
<b>21 - 24</b>	$(20.9 \pm 0.17^{+10.5}_{-10.5}) \times 10^6$	$(20.3 \pm 0.17^{+10.1}_{-10.1}) \times 10^6$
<b>24 - 28</b>	$(11.4 \pm 0.13^{+4.84}_{-4.85}) \times 10^6$	$(11.1 \pm 0.13^{+4.57}_{-4.57}) \times 10^6$
<b>28 - 32</b>	$(4.58 \pm 0.07^{+1.61}_{-1.61}) \times 10^6$	$(4.64 \pm 0.07^{+1.51}_{-1.51}) \times 10^6$
<b>32 - 37</b>	$(2.30 \pm 0.06^{+0.67}_{-0.67}) \times 10^6$	$(2.25 \pm 0.06^{+0.63}_{-0.63}) \times 10^6$
<b>37 - 43</b>	$(1.11 \pm 0.04^{+0.26}_{-0.26}) \times 10^6$	$(1.12 \pm 0.04^{+0.26}_{-0.26}) \times 10^6$
<b>43 - 49</b>	$(0.52 \pm 0.02^{+0.10}_{-0.10}) \times 10^6$	$(0.55 \pm 0.02^{+0.10}_{-0.10}) \times 10^6$
<b>49 - 56</b>	$(2.99 \pm 0.19^{+0.46}_{-0.47}) \times 10^5$	$(3.21 \pm 0.19^{+0.50}_{-0.50}) \times 10^5$
<b>56 - 64</b>	$(1.60 \pm 0.13^{+0.20}_{-0.20}) \times 10^5$	$(1.65 \pm 0.12^{+0.21}_{-0.21}) \times 10^5$
<b>64 - 74</b>	$(0.82 \pm 0.06^{+0.08}_{-0.08}) \times 10^5$	$(0.83 \pm 0.06^{+0.09}_{-0.09}) \times 10^5$

Table 2: The  $p_T$  differential cross section corrected to hadron level for inclusive jets at  $1 < |y| < 1.5$  and  $1.5 < |y| < 2$ . The first (second) uncertainty reflects the statistical (systematic) contribution.

$p_T$ [GeV/c]	$\frac{d^2\sigma}{dp_T dy}$ [pb/(GeV/c)] $1 <  y  < 1.5$	$\frac{d^2\sigma}{dp_T dy}$ [pb/(GeV/c)] $1.5 <  y  < 2$
<b>21 - 24</b>	$(17.9 \pm 0.16^{+8.46}_{-8.43}) \times 10^6$	$(15.9 \pm 0.15^{+6.76}_{-6.83}) \times 10^6$
<b>24 - 28</b>	$(9.69 \pm 0.11^{+4.00}_{-4.00}) \times 10^6$	$(8.50 \pm 0.10^{+3.23}_{-3.22}) \times 10^6$
<b>28 - 32</b>	$(3.68 \pm 0.07^{+1.31}_{-1.30}) \times 10^6$	$(3.32 \pm 0.06^{+1.10}_{-1.10}) \times 10^6$
<b>32 - 37</b>	$(1.80 \pm 0.05^{+0.54}_{-0.54}) \times 10^6$	$(1.66 \pm 0.05^{+0.47}_{-0.47}) \times 10^6$
<b>37 - 43</b>	$(0.88 \pm 0.03^{+0.22}_{-0.22}) \times 10^6$	$(0.79 \pm 0.03^{+0.19}_{-0.19}) \times 10^6$
<b>43 - 49</b>	$(4.20 \pm 0.20^{+0.84}_{-0.82}) \times 10^5$	$(3.61 \pm 0.19^{+0.70}_{-0.70}) \times 10^5$
<b>49 - 56</b>	$(2.33 \pm 0.16^{+0.35}_{-0.36}) \times 10^5$	$(1.96 \pm 0.15^{+0.29}_{-0.30}) \times 10^5$
<b>56 - 64</b>	$(1.17 \pm 0.09^{+0.13}_{-0.13}) \times 10^5$	$(0.94 \pm 0.09^{+0.10}_{-0.10}) \times 10^5$
<b>64 - 74</b>	$(0.61 \pm 0.05^{+0.05}_{-0.05}) \times 10^5$	$(0.47 \pm 0.05^{+0.03}_{-0.03}) \times 10^5$

Table 3: The  $p_T$  differential cross section corrected to hadron level for inclusive jets at  $2 < |y| < 2.5$ ,  $2.5 < |y| < 3$  and  $3.2 < |y| < 4.7$ . The first (second) uncertainty reflects the statistical (systematic) contribution.

$p_T$ [GeV/c]	$\frac{d^2\sigma}{dp_T dy}$ [pb/(GeV/c)] $2 <  y  < 2.5$	$\frac{d^2\sigma}{dp_T dy}$ [pb/(GeV/c)] $2.5 <  y  < 3$	$\frac{d^2\sigma}{dp_T dy}$ [pb/(GeV/c)] $3.2 <  y  < 4.7$
<b>21 - 24</b>	$(12.8 \pm 0.15^{+6.47}_{-5.10}) \times 10^6$	$(9.37 \pm 0.11^{+5.53}_{-5.40}) \times 10^6$	$(4.04 \pm 0.05^{+2.08}_{-2.11}) \times 10^6$
<b>24 - 28</b>	$(7.07 \pm 0.11^{+3.10}_{-2.62}) \times 10^6$	$(5.20 \pm 0.08^{+2.65}_{-2.39}) \times 10^6$	$(2.02 \pm 0.03^{+0.86}_{-0.87}) \times 10^6$
<b>28 - 32</b>	$(2.84 \pm 0.06^{+1.09}_{-0.97}) \times 10^6$	$(1.98 \pm 0.05^{+0.88}_{-0.78}) \times 10^6$	$(0.78 \pm 0.02^{+0.27}_{-0.28}) \times 10^6$
<b>32 - 37</b>	$(1.38 \pm 0.05^{+0.48}_{-0.44}) \times 10^6$	$(0.92 \pm 0.04^{+0.37}_{-0.33}) \times 10^6$	$(0.39 \pm 0.02^{+0.12}_{-0.12}) \times 10^6$
<b>37 - 43</b>	$(6.51 \pm 0.36^{+2.04}_{-1.95}) \times 10^5$	$(4.50 \pm 0.26^{+1.66}_{-1.49}) \times 10^5$	$(1.74 \pm 0.10^{+0.47}_{-0.48}) \times 10^5$
<b>43 - 49</b>	$(2.97 \pm 0.20^{+0.86}_{-0.83}) \times 10^5$	$(2.14 \pm 0.15^{+0.72}_{-0.66}) \times 10^5$	$(0.65 \pm 0.05^{+0.16}_{-0.16}) \times 10^5$
<b>49 - 56</b>	$(1.36 \pm 0.14^{+0.37}_{-0.36}) \times 10^5$	$(1.18 \pm 0.12^{+0.37}_{-0.34}) \times 10^5$	$(0.27 \pm 0.03^{+0.07}_{-0.07}) \times 10^5$
<b>56 - 64</b>	$(6.48 \pm 0.86^{+1.68}_{-1.62}) \times 10^4$	$(6.36 \pm 0.78^{+1.84}_{-1.74}) \times 10^4$	$(1.14 \pm 0.18^{+0.29}_{-0.29}) \times 10^4$
<b>64 - 74</b>	$(4.32 \pm 0.53^{+1.08}_{-1.04}) \times 10^4$	$(3.01 \pm 0.38^{+0.81}_{-0.77}) \times 10^4$	$(0.61 \pm 0.10^{+0.18}_{-0.18}) \times 10^4$

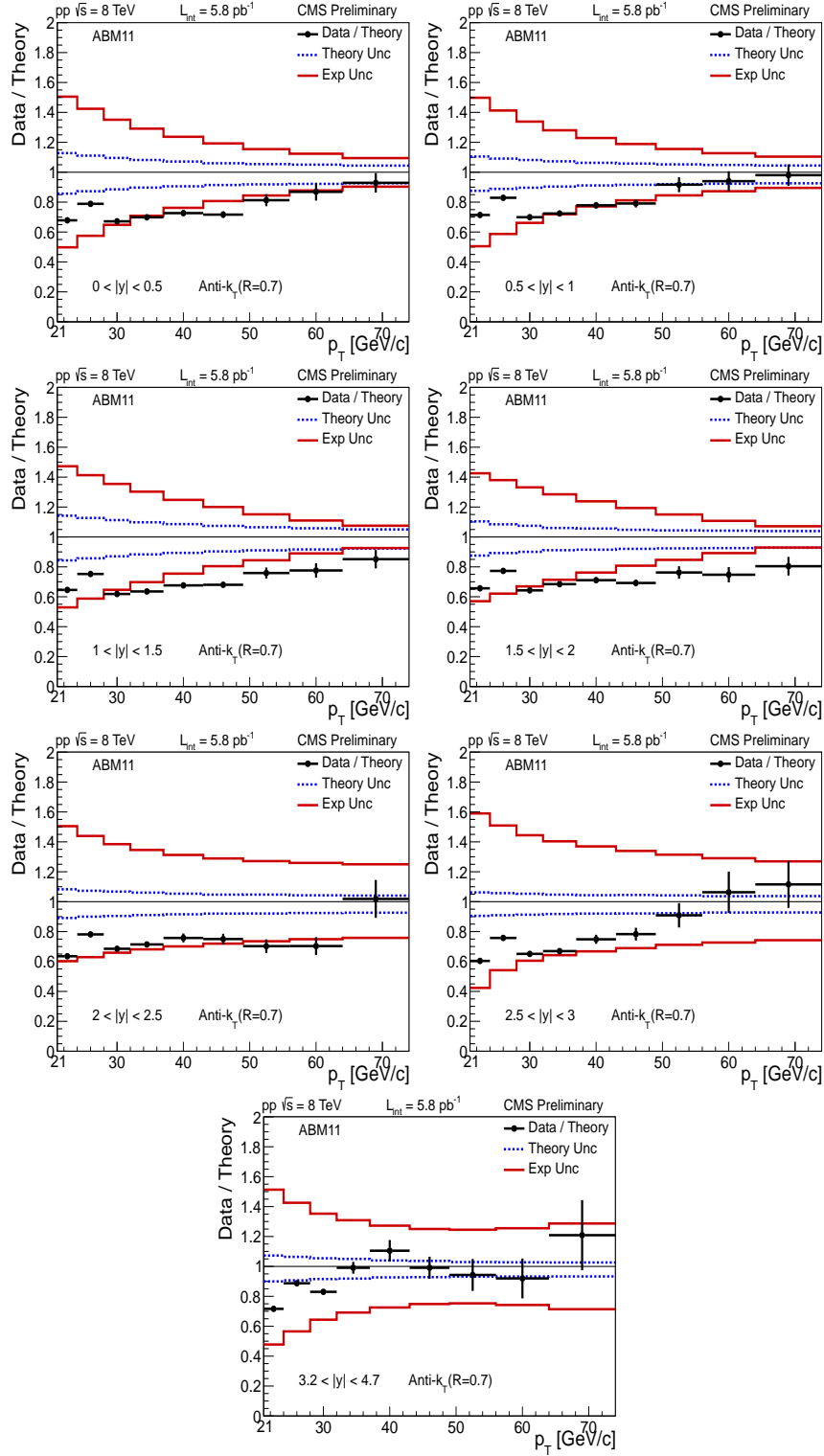


Figure 2: Inclusive jet cross sections for data over the theoretical prediction of the ABM11 PDF set for all  $|y|$ . The experimental and theoretical systematic uncertainties are represented by the continuous and dashed lines, respectively.

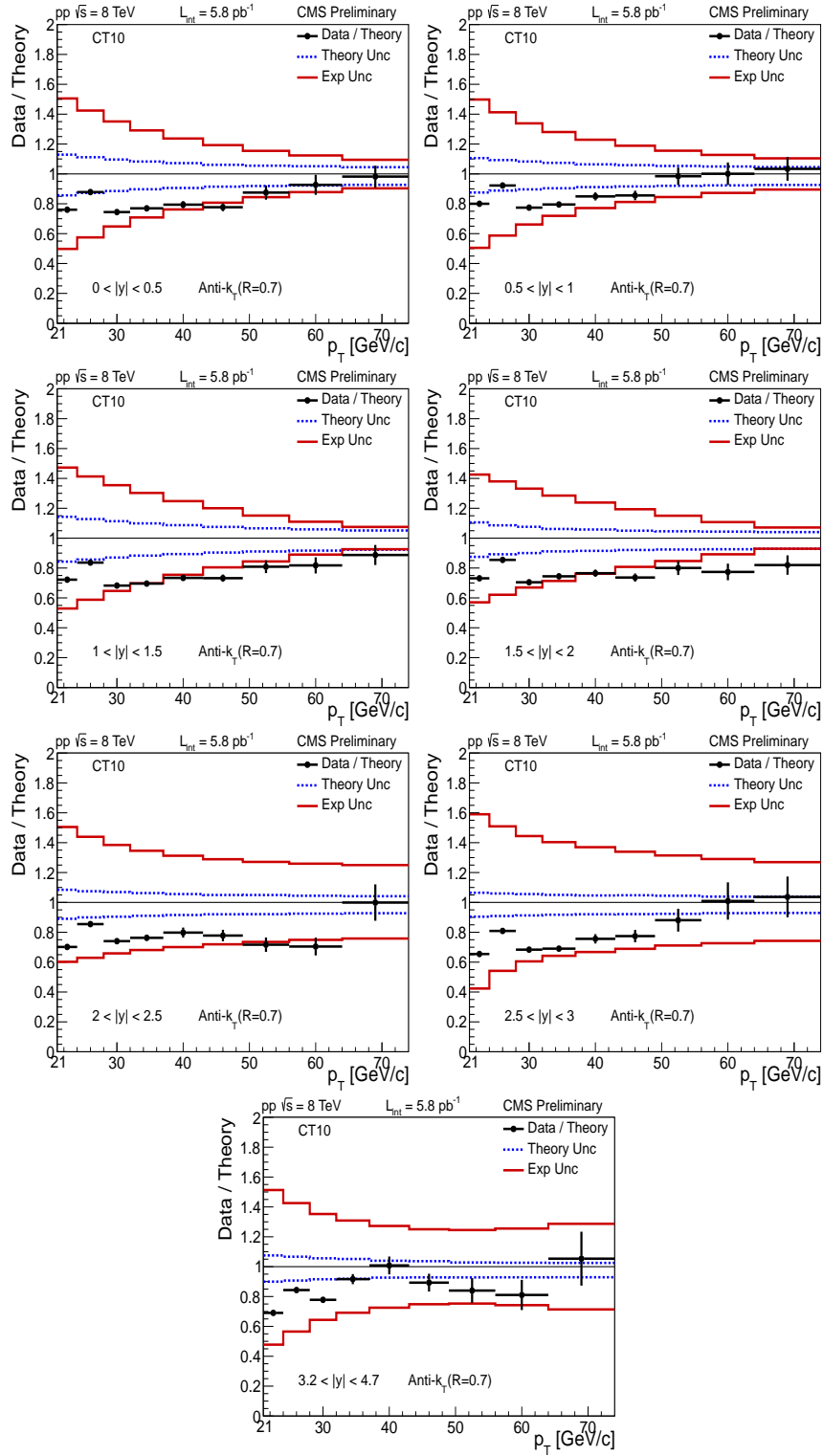


Figure 3: Inclusive jet cross sections for data over the theoretical prediction of the CT10 PDF set for all  $|y|$ . The experimental and theoretical systematic uncertainties are represented by the continuous and dashed lines, respectively.

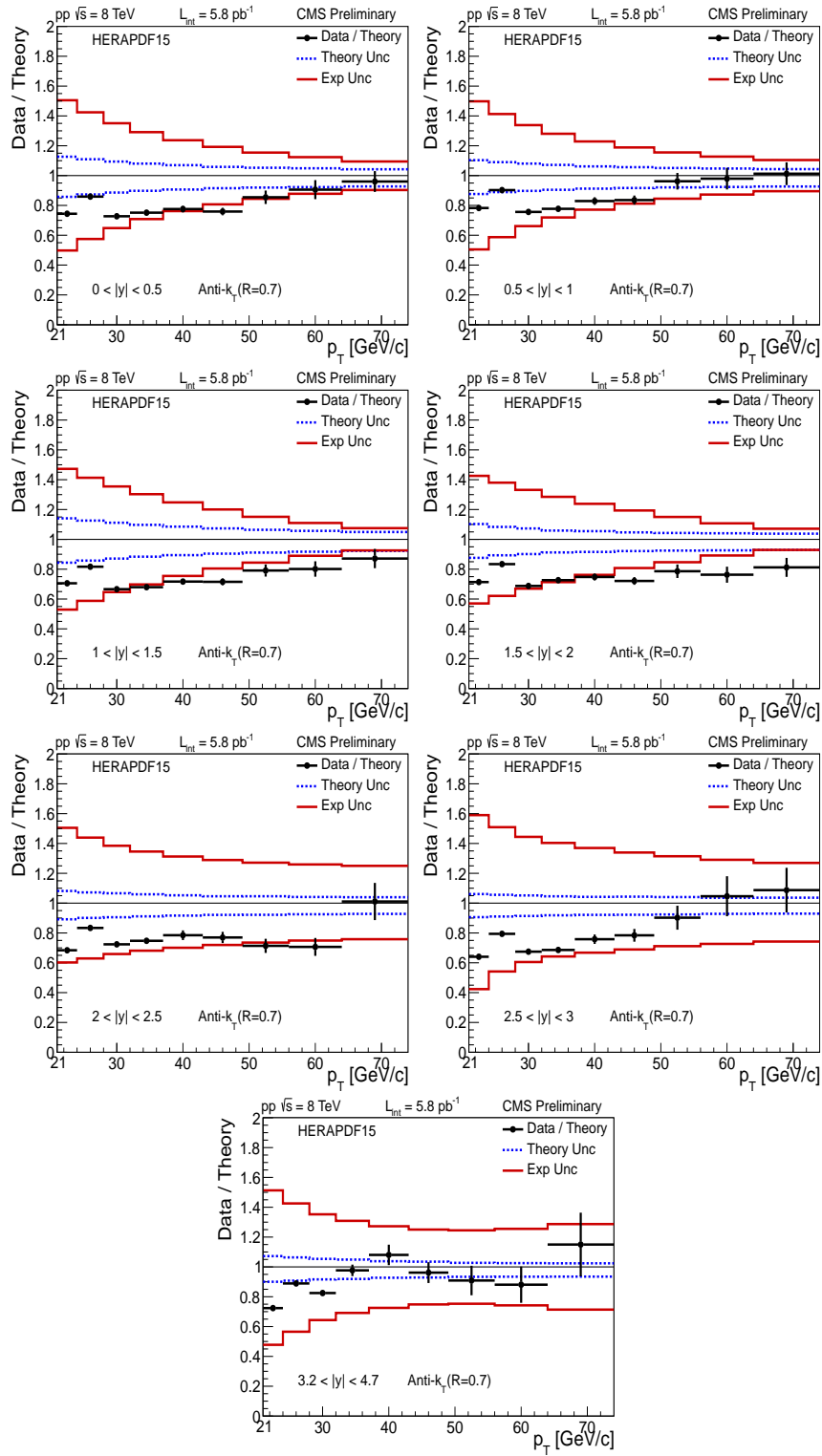


Figure 4: Inclusive jet cross sections for data over the theoretical prediction of the HERAPDF1.5 PDF set for all  $|y|$ . The experimental and theoretical systematic uncertainties are represented by the continuous and dashed lines, respectively.

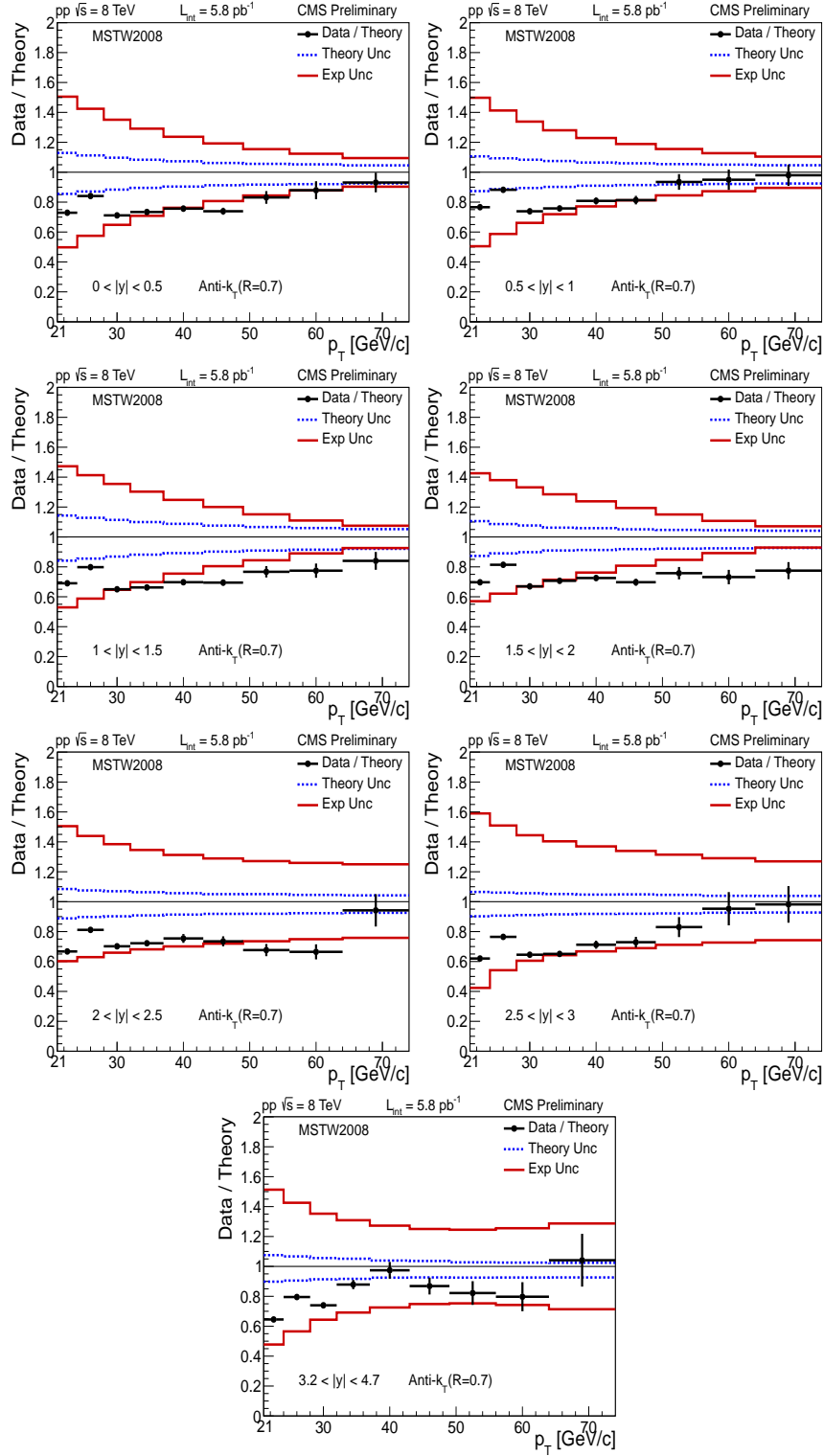


Figure 5: Inclusive jet cross sections for data over the theoretical prediction of the MSTW2008 PDF set for all  $|y|$ . The experimental and theoretical systematic uncertainties are represented by the continuous and dashed lines, respectively.

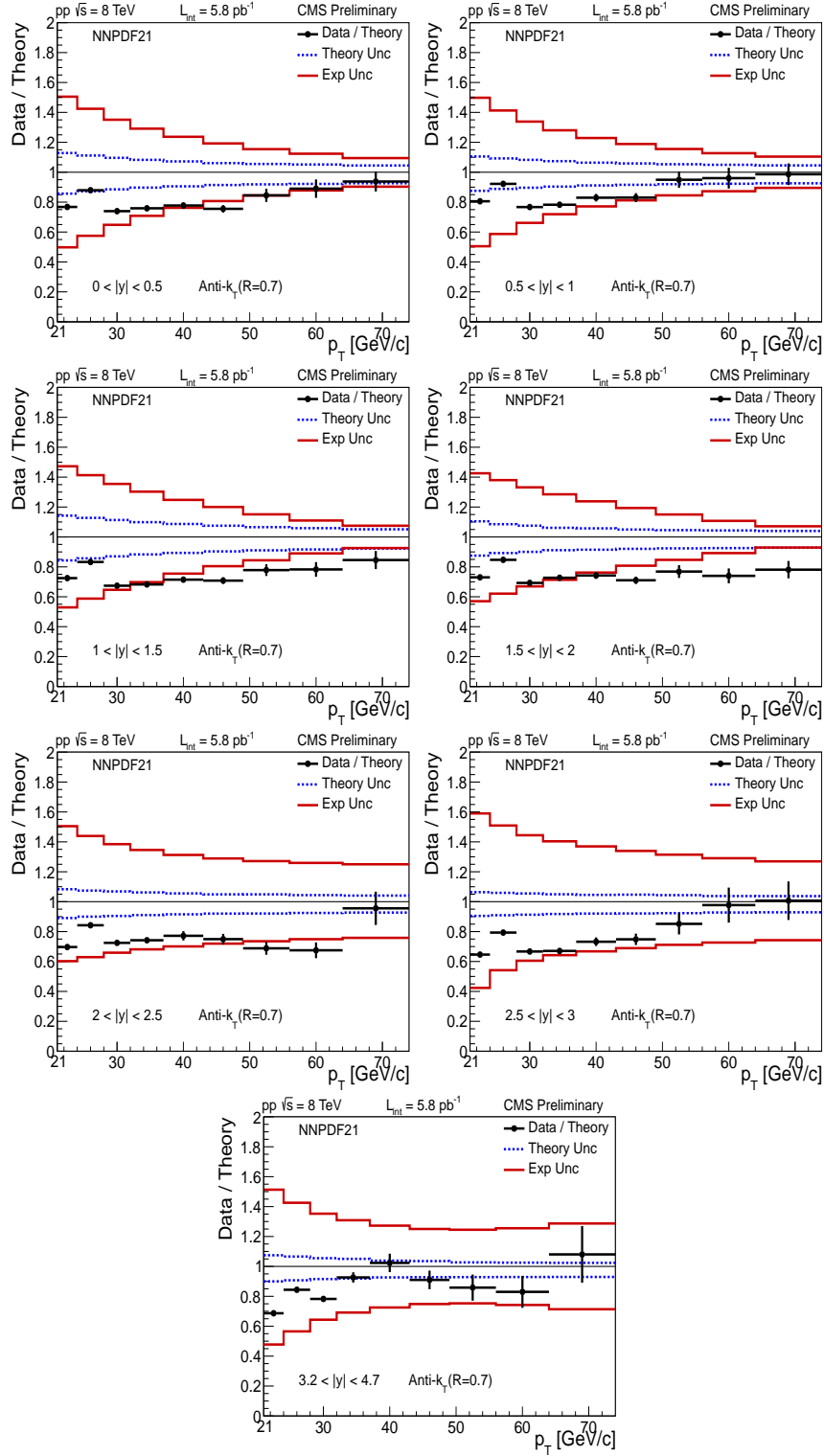


Figure 6: Inclusive jet cross sections for data over the theoretical prediction of the NNPDF2.1 PDF set for all  $|y|$ . The experimental and theoretical systematic uncertainties are represented by the continuous and dashed lines, respectively.

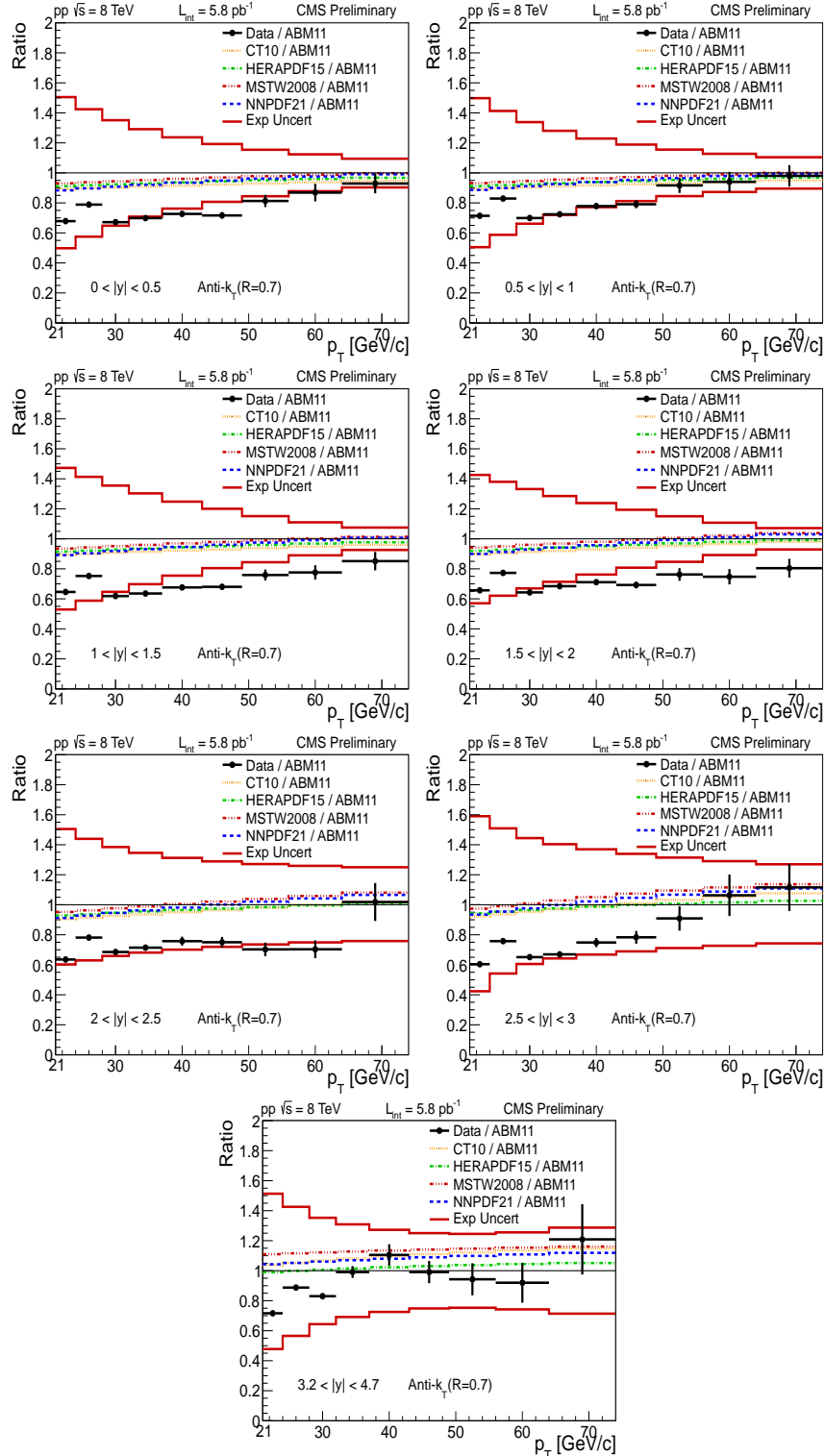


Figure 7: Ratio of inclusive jet cross sections to the theoretical prediction using the central value of the ABM11 PDF set for all  $|y|$  bins. The dashed lines show the ratio of the cross sections calculated with the other PDF sets to that calculated with ABM11. The experimental uncertainty is represented by the continuous line.



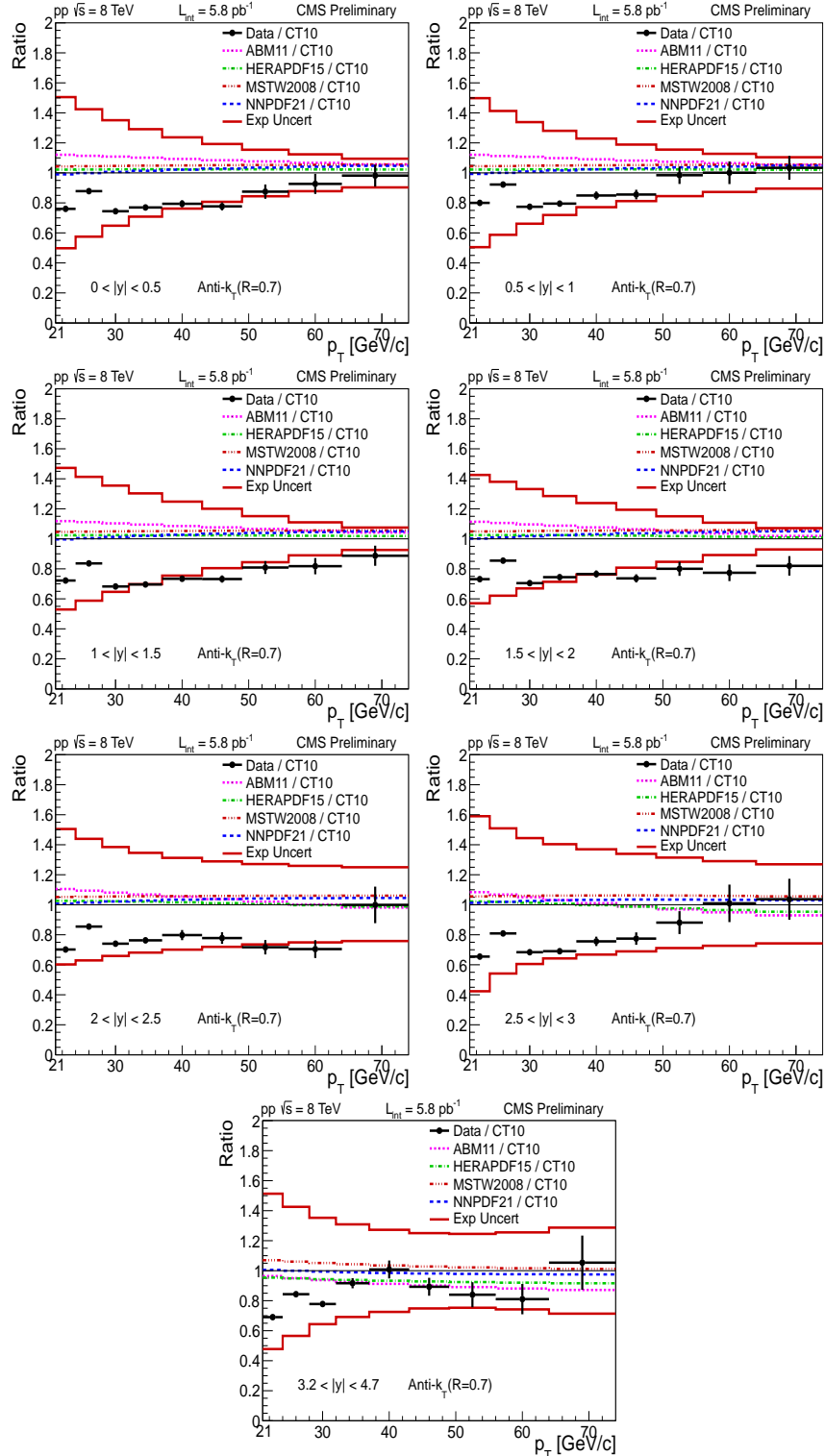


Figure 8: Ratio of inclusive jet cross sections to the theoretical prediction using the central value of the CT10 PDF set for all  $|y|$  bins. The dashed lines show the ratio of the cross sections calculated with the other PDF sets to that calculated with CT10. The experimental uncertainty is represented by the continuous line.

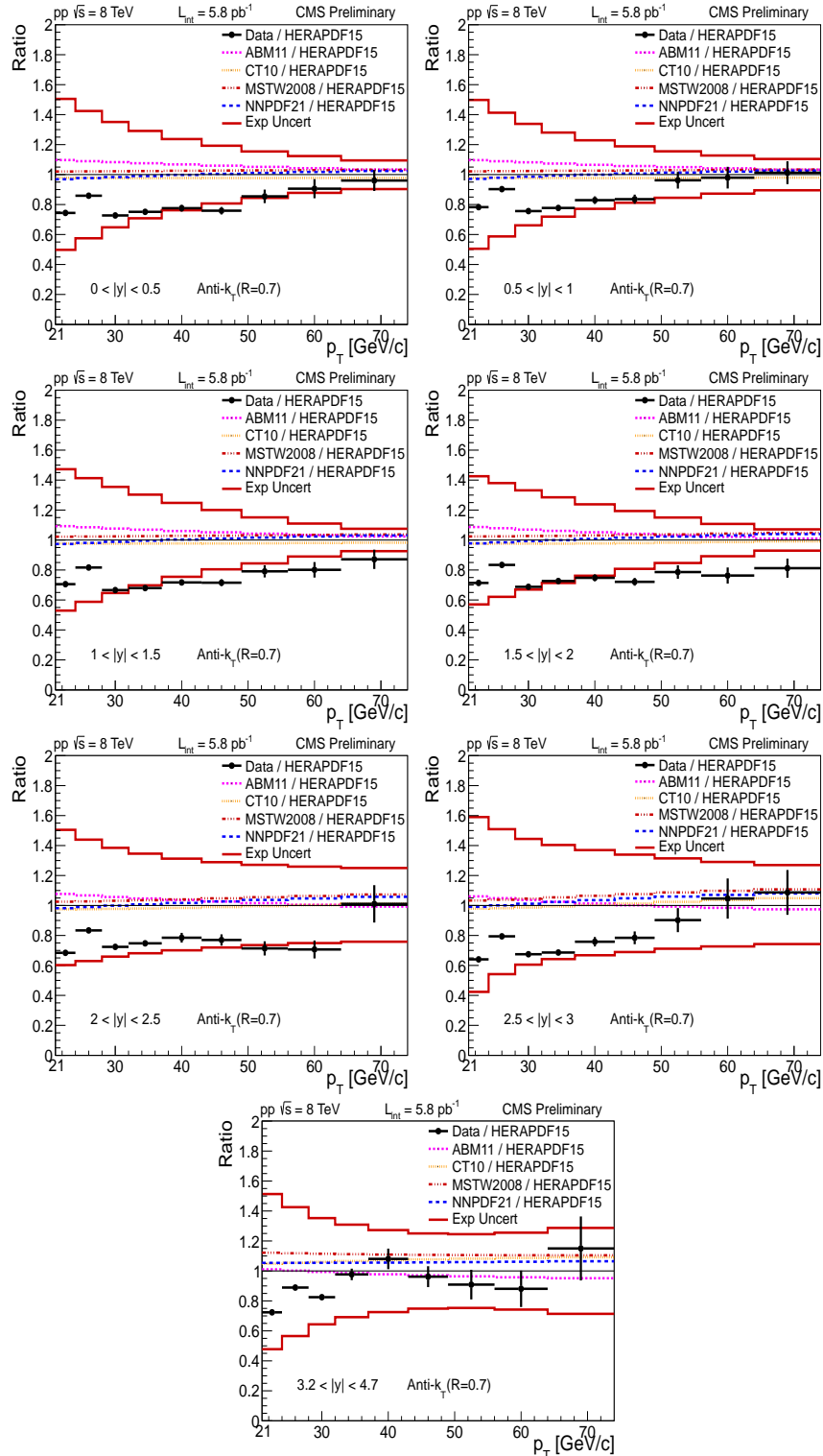


Figure 9: Ratio of inclusive jet cross sections to the theoretical prediction using the central value of the HERAPDF1.5 PDF set for all  $|y|$  bins. The dashed lines show the ratio of the cross sections calculated with the other PDF sets to that calculated with HERAPDF1.5. The experimental uncertainty is represented by the continuous line.

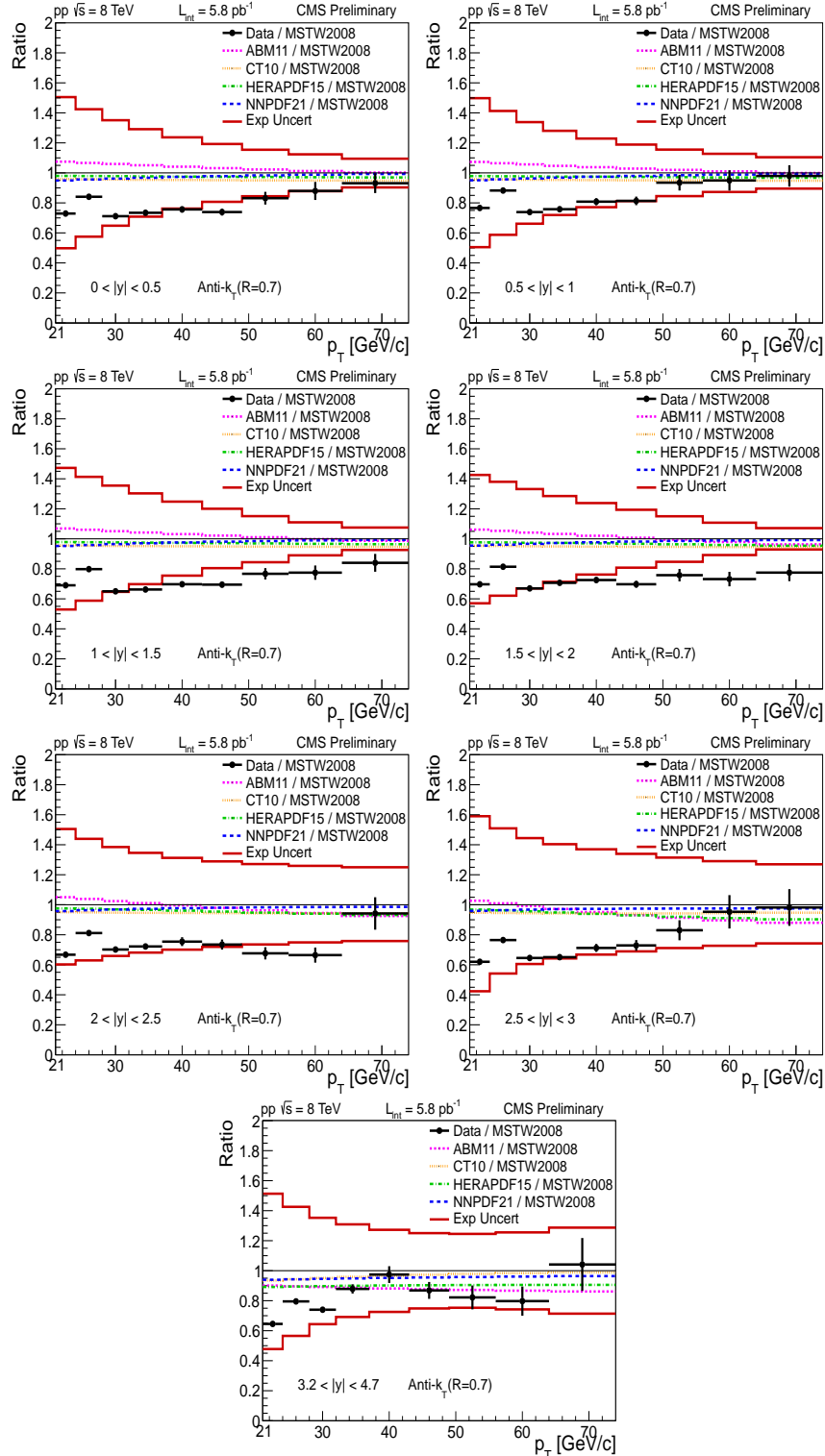


Figure 10: Ratio of inclusive jet cross sections to the theoretical prediction using the central value of the MSTW2008 PDF set for all  $|y|$  bins. The dashed lines show the ratio of the cross sections calculated with the other PDF sets to that calculated with MSTW2008. The experimental uncertainty is represented by the continuous line.

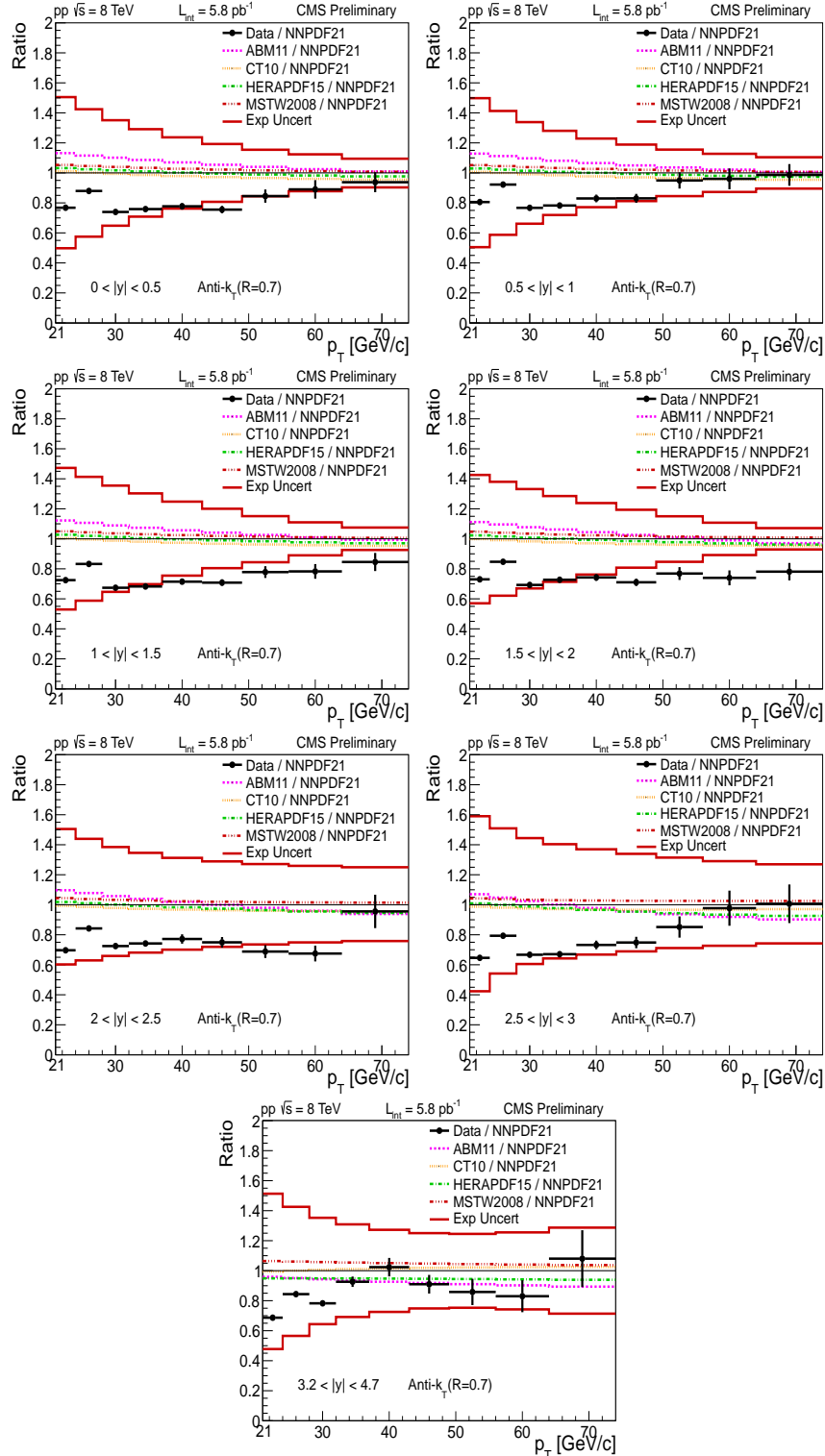


Figure 11: Ratio of inclusive jet cross sections to the theoretical prediction using the central value of the NNPDF2.1 PDF set for all  $|y|$  bins. The dashed lines show the ratio of the cross sections calculated with the other PDF sets to that calculated with NNPDF2.1. The experimental uncertainty is represented by the continuous line.

## 10 Appendix

The combined differential inclusive jet cross sections, measured at low and high transverse momenta [25], in comparison to NLO predictions using the NNPDF2.1 PDF set times the NP correction factor is shown in Fig. 12.

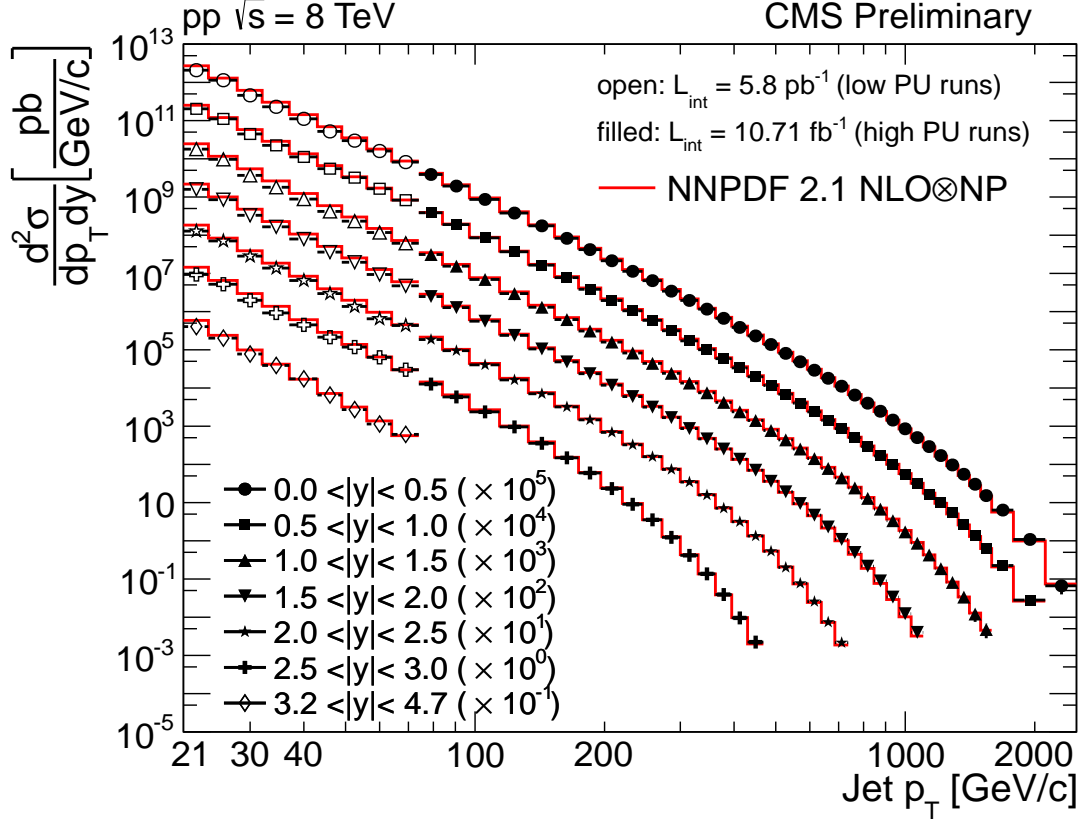


Figure 12: The combined differential inclusive jet cross sections in comparison to NLO predictions using the NNPDF2.1 PDF set times the NP correction factor. Open markers represent the measurement of low  $p_T$  jets obtained with the integrated luminosity of  $5.8 \text{ pb}^{-1}$  of minimum bias data for low pile-up conditions whereas the filled markers for high  $p_T$  jets obtained with integrated luminosity of  $10.71 \text{ fb}^{-1}$  of jet trigger data for high pileup [25].

Ratio of the combined CMS jet spectra, measured at low and high transverse momenta, over the NLO predictions is shown in Figs. 13–17. In the transition between both measurements at  $p_T \approx 75 \text{ GeV}/c$ , the systematic uncertainties of the low- $p_T$  measurements are smaller than the high- $p_T$  ones because the former have been carried out with (much) smaller pileup than the latter, except for the  $2 < |y| < 3$  region where the endcap response to low- $p_T$  jets results in larger propagated systematics. A similar comparison but instead of the theoretical uncertainty for each PDF set the ratios of the predictions with alternative PDF sets is shown in Figs. 18–22.

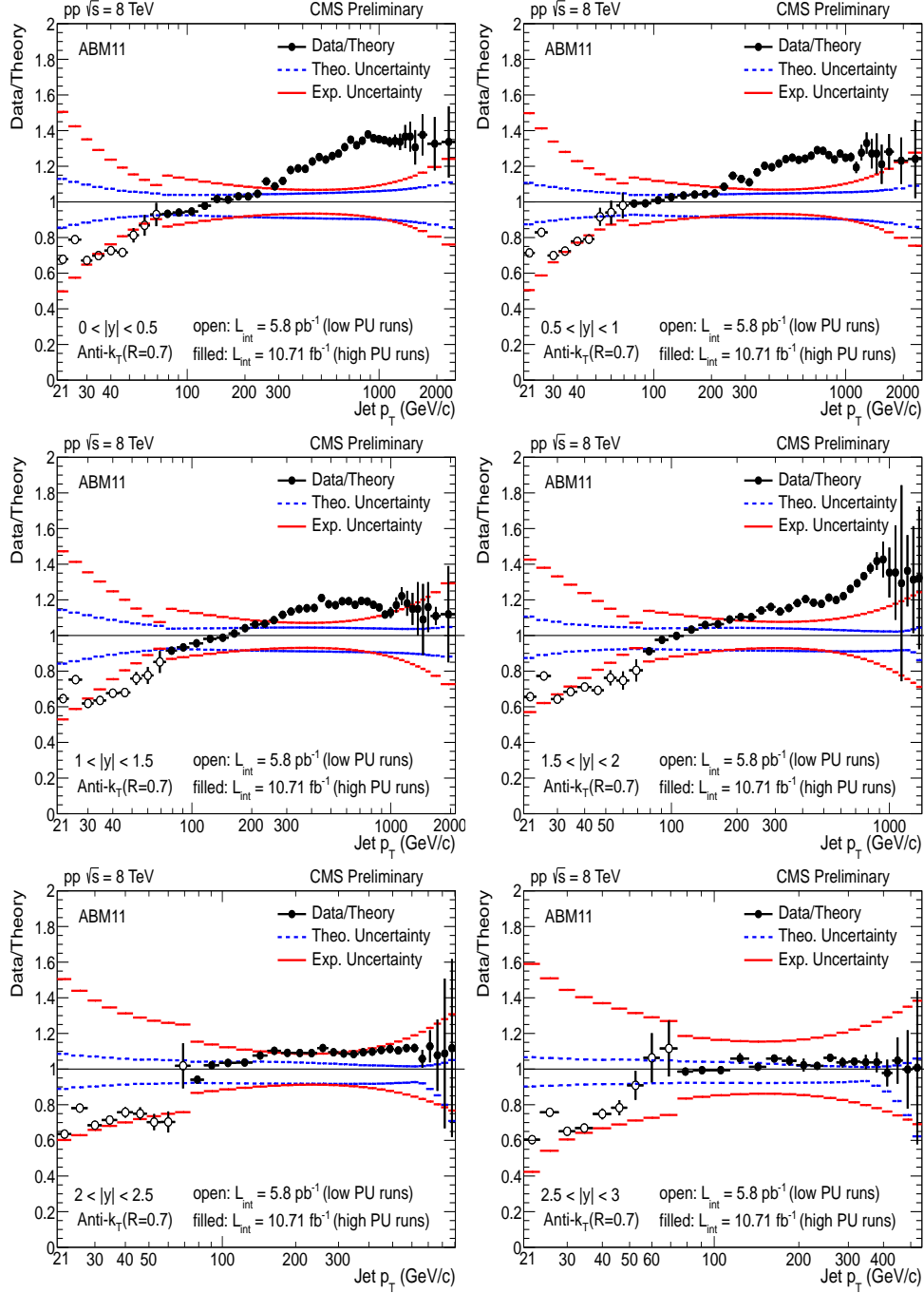


Figure 13: The combined results both for low and high  $p_T$  jets [25]. Ratio of data to the theoretical prediction of the ABM11 PDF set. The experimental uncertainty and the theoretical uncertainty are represented by the continuous and dashed line, respectively. The error bars correspond to the statistical uncertainty of the data.

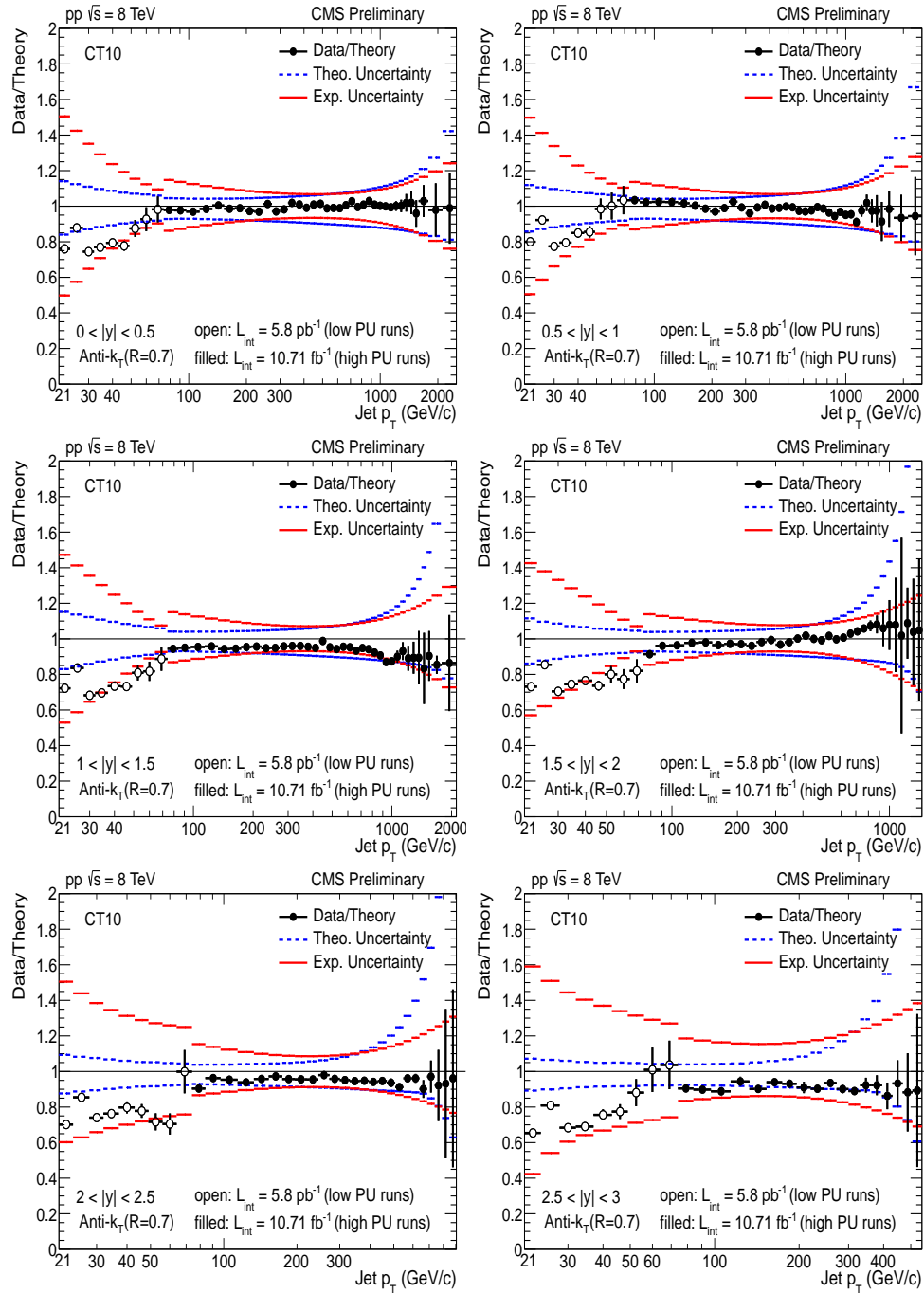


Figure 14: The combined results both for low and high  $p_T$  jets [25]. Ratio of data to the theoretical prediction of the CT10 PDF set. The experimental uncertainty and the theoretical uncertainty are represented by the continuous and dashed line, respectively. The error bars correspond to the statistical uncertainty of the data.

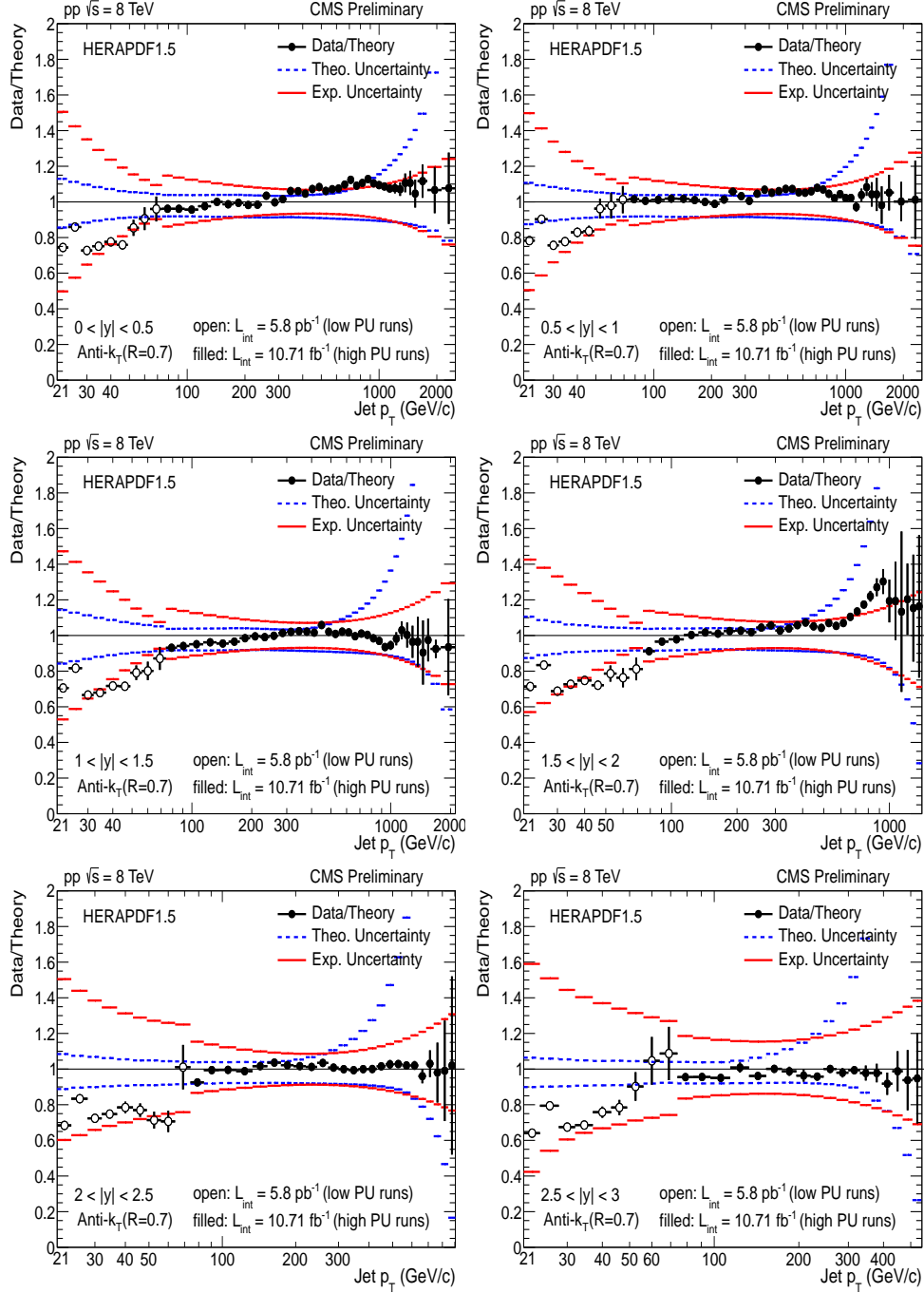


Figure 15: The combined results both for low and high  $p_T$  jets [25]. Ratio of data to the theoretical prediction of the HERAPDF1.5 PDF set. The experimental uncertainty and the theoretical uncertainty are represented by the continuous and dashed line, respectively. The error bars correspond to the statistical uncertainty of the data.



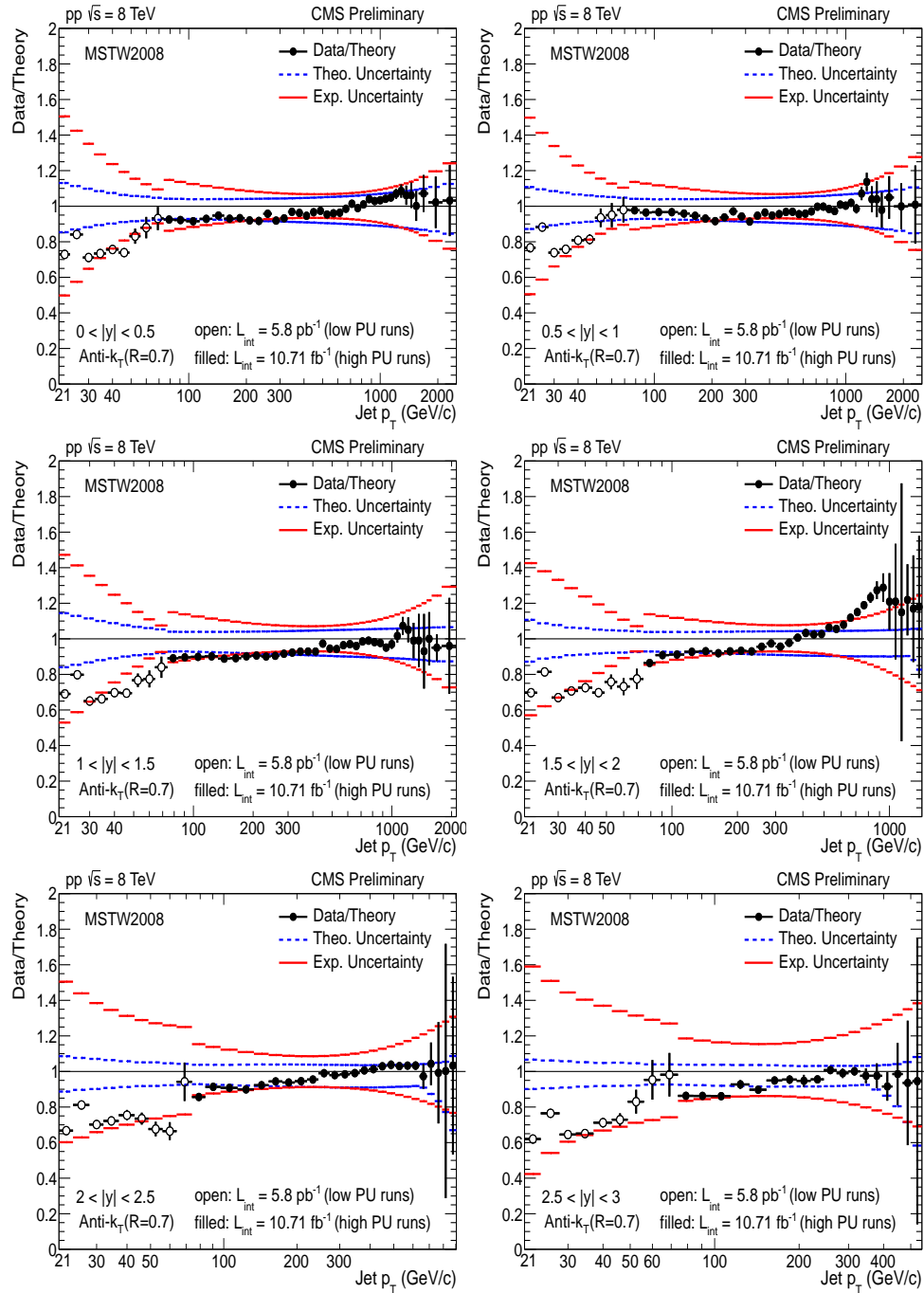


Figure 16: The combined results both for low and high  $p_T$  jets [25]. Ratio of data to the theoretical prediction of the MSTW2008 PDF set. The experimental uncertainty and the theoretical uncertainty are represented by the continuous and dashed line, respectively. The error bars correspond to the statistical uncertainty of the data.

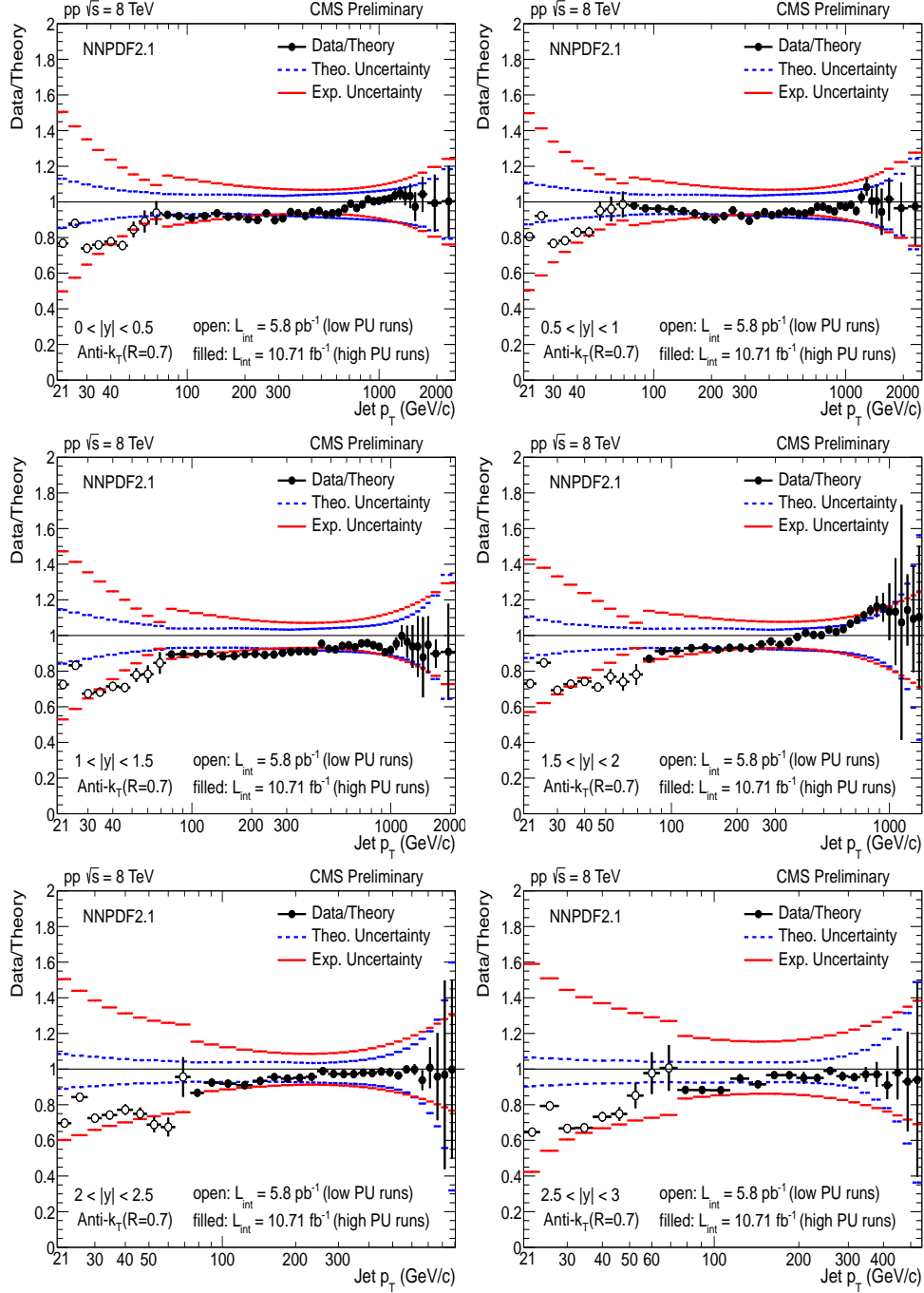


Figure 17: The combined results both for low and high  $p_T$  jets [25]. Ratio of data to the theoretical prediction of the NNPDF2.1 PDF set. The experimental uncertainty and the theoretical uncertainty are represented by the continuous and dashed line, respectively. The error bars correspond to the statistical uncertainty of the data.

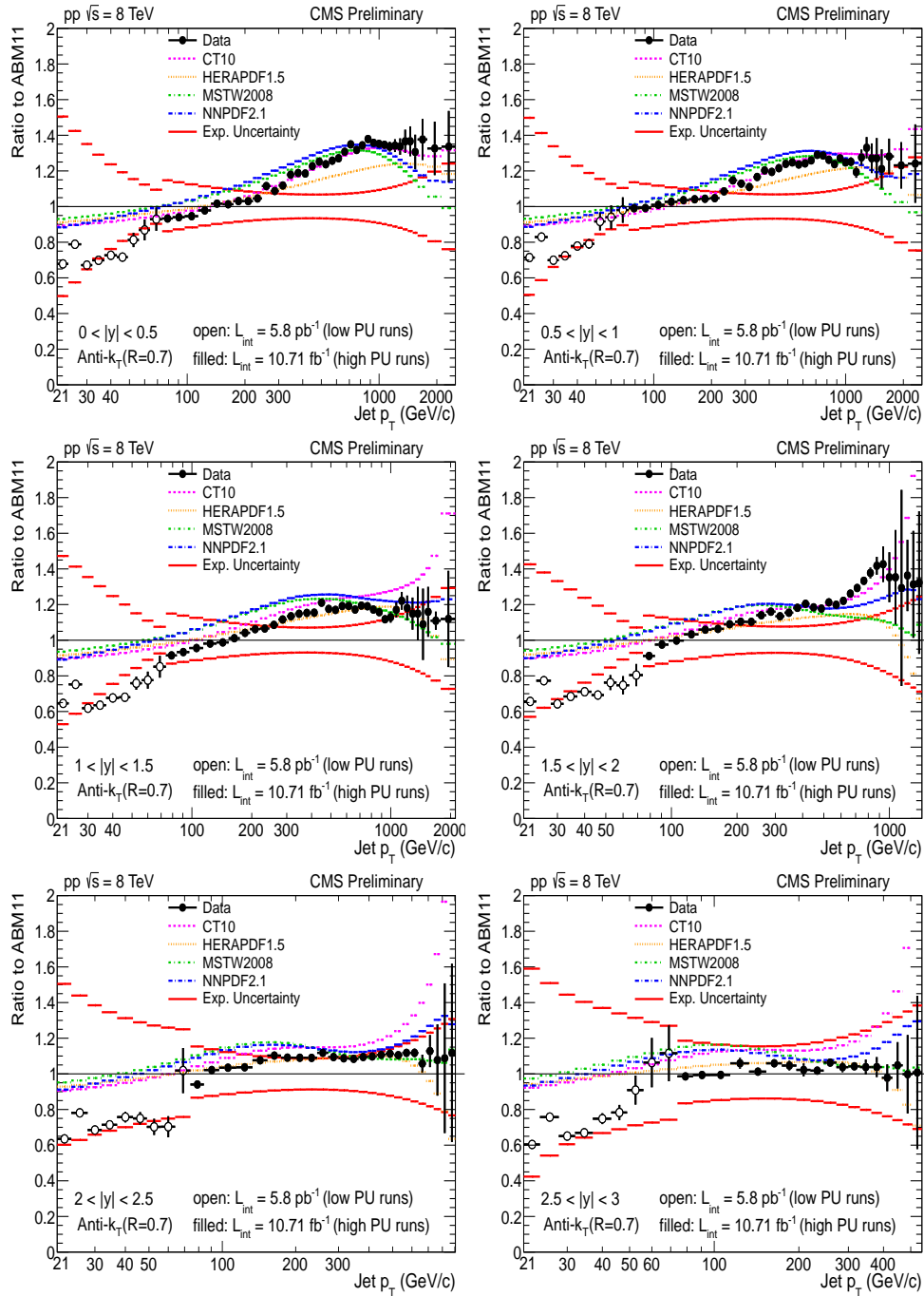


Figure 18: The combined results both for low and high  $p_T$  jets [25]. Ratio of inclusive jet cross sections to the theoretical prediction using the central value of the ABM11 PDF set for all  $|y|$  bins. The experimental uncertainty is represented by the continuous line.

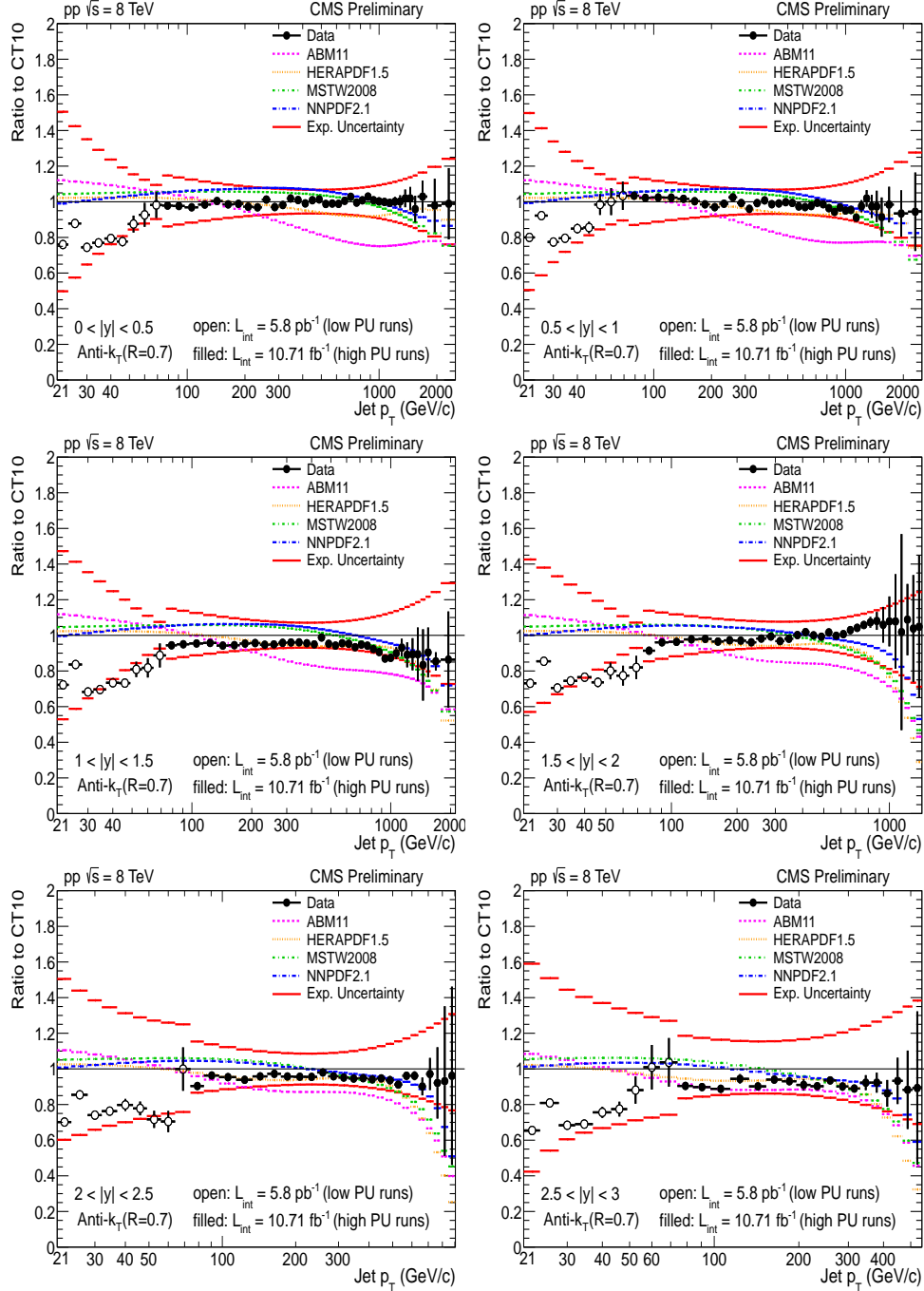


Figure 19: The combined results both for low and high  $p_T$  jets [25]. Ratio of inclusive jet cross sections to the theoretical prediction using the central value of the CT10 PDF set for all  $|y|$  bins. The experimental uncertainty is represented by the continuous line.

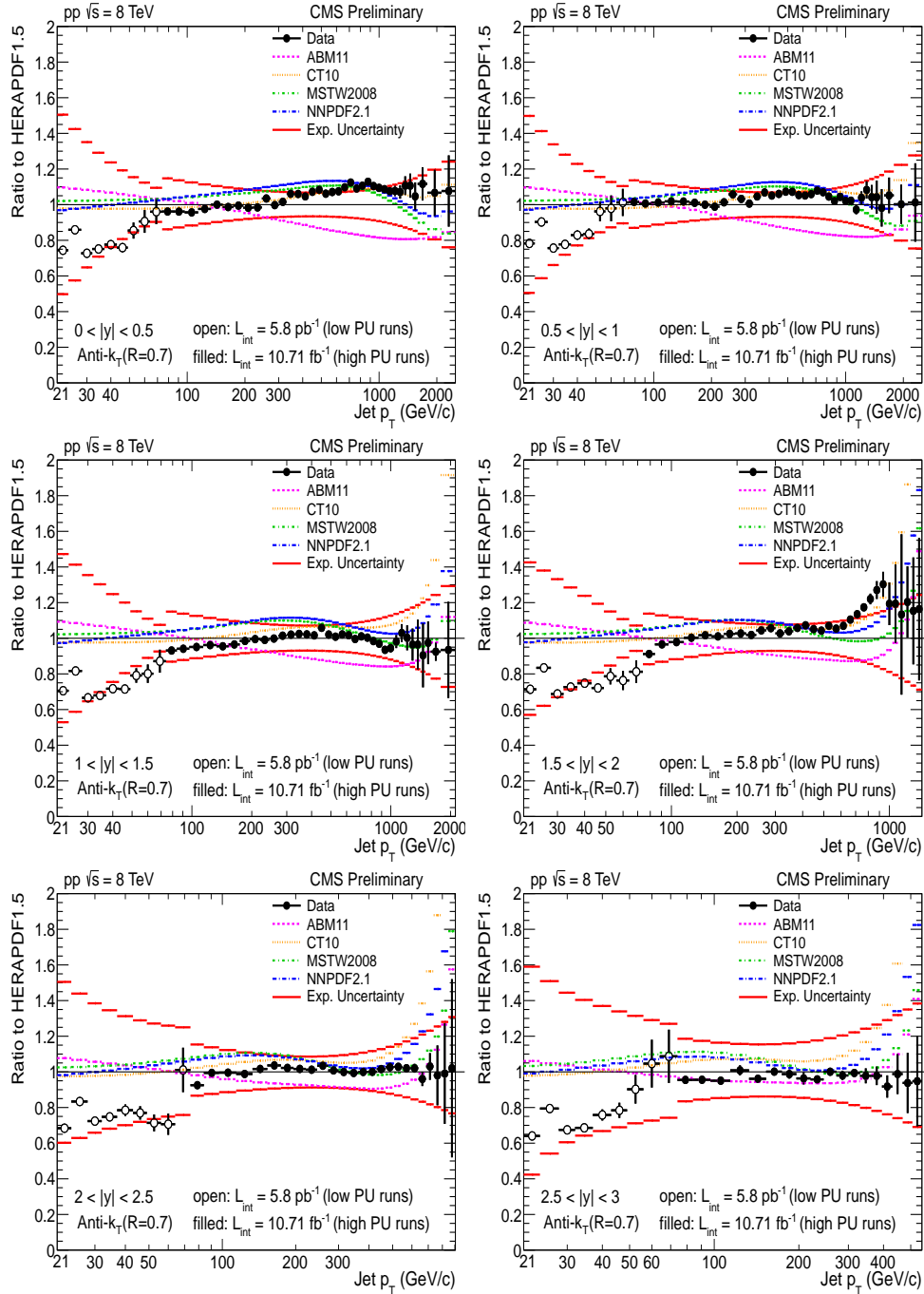


Figure 20: The combined results both for low and high  $p_T$  jets [25]. Ratio of inclusive jet cross sections to the theoretical prediction using the central value of the HERAPDF1.5 PDF set for all  $|y|$  bins. The experimental uncertainty is represented by the continuous line.

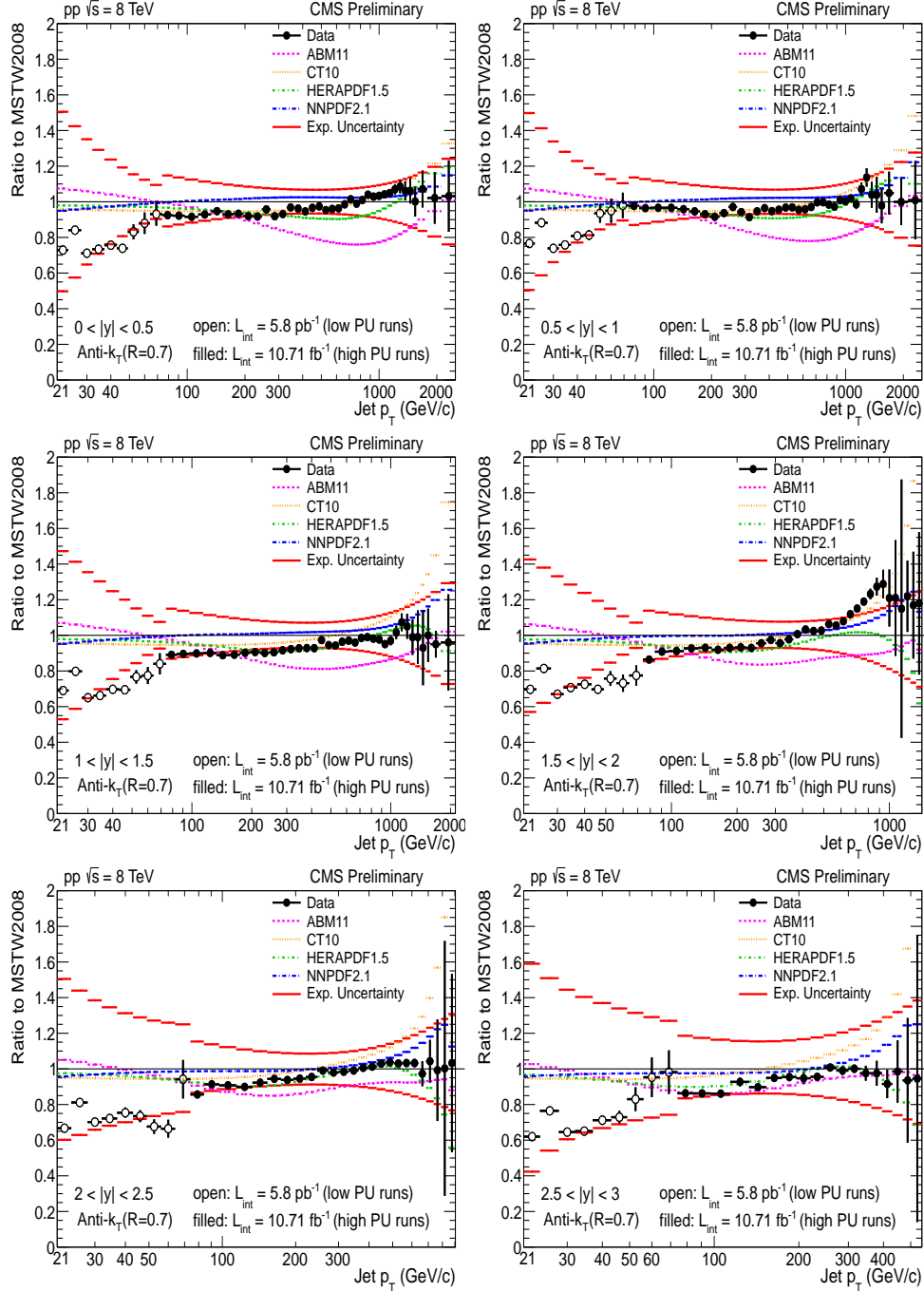


Figure 21: The combined results both for low and high  $p_T$  jets [25]. Ratio of inclusive jet cross sections to the theoretical prediction using the central value of the MSTW2008 PDF set for all  $|y|$  bins. The experimental uncertainty is represented by the continuous line.

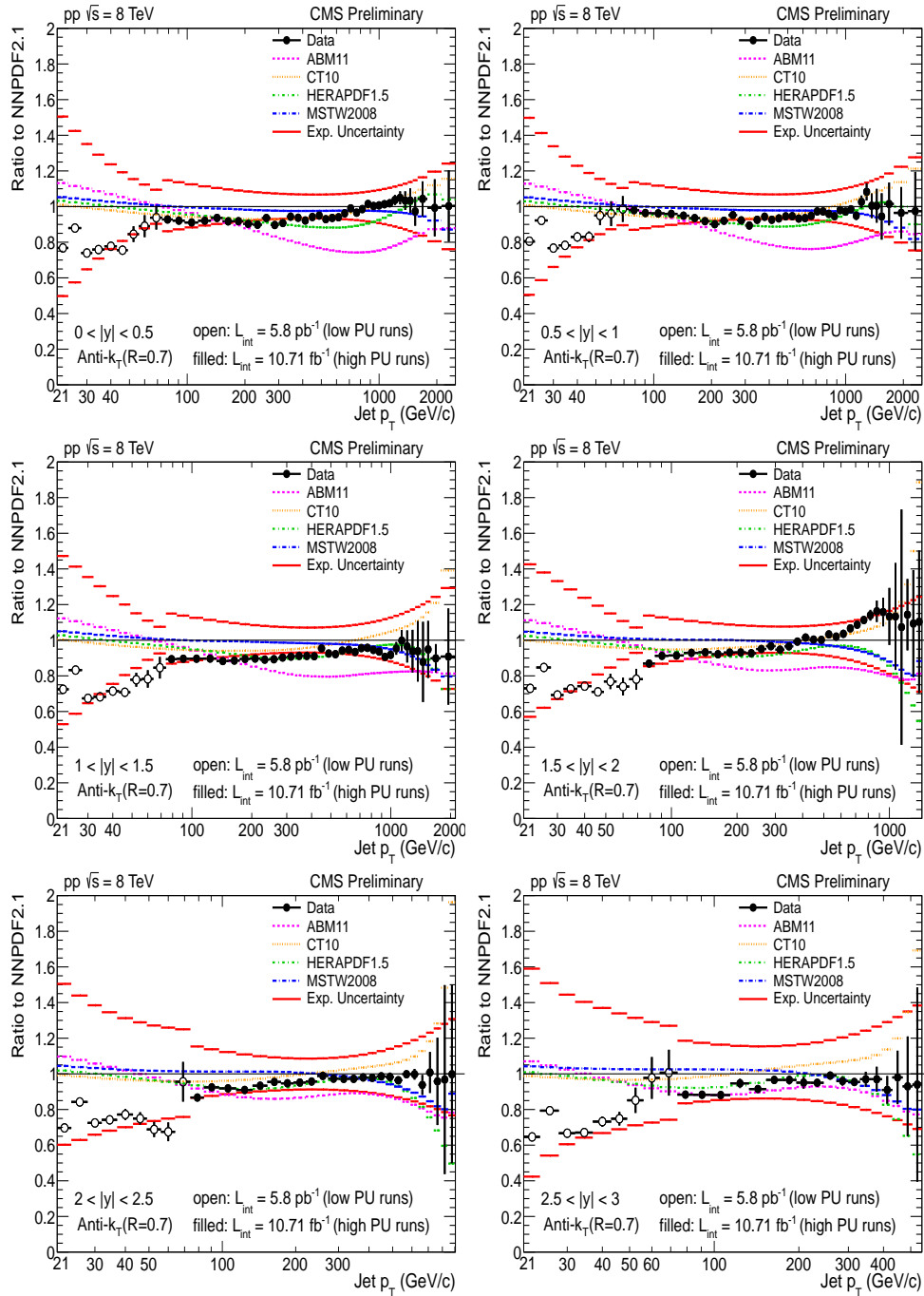


Figure 22: The combined results both for low and high  $p_T$  jets [25]. Ratio of inclusive jet cross sections to the theoretical prediction using the central value of the NNPDF2.1 PDF set for all  $|y|$  bins. The experimental uncertainty is represented by the continuous line.

## References

- [1] ATLAS Collaboration, “Measurement of inclusive jet and dijet production in  $pp$  collisions at  $\sqrt{s} = 7$  TeV using the ATLAS detector”, *Phys.Rev.* **D86** (2012) 014022, doi:10.1103/PhysRevD.86.014022, arXiv:1112.6297.
- [2] CMS Collaboration, “Measurement of the Inclusive Jet Cross Section in  $pp$  Collisions at  $\sqrt{s} = 7$  TeV”, *Phys.Rev.Lett.* **107** (2011) 132001, doi:10.1103/PhysRevLett.107.132001, arXiv:1106.0208.
- [3] CMS Collaboration, “Measurements of differential jet cross sections in proton-proton collisions at  $\sqrt{s} = 7$  TeV with the CMS detector”, arXiv:1212.6660.
- [4] M. Deak, F. Hautmann, H. Jung, and K. Kutak, “Forward Jet Production at the Large Hadron Collider”, *JHEP* **0909** (2009) 121, doi:10.1088/1126-6708/2009/09/121, arXiv:0908.0538.
- [5] M. Deak, F. Hautmann, H. Jung, and K. Kutak, “Forward-Central Jet Correlations at the Large Hadron Collider”, arXiv:1012.6037.
- [6] M. Deak, F. Hautmann, H. Jung, and K. Kutak, “Forward Jets and Energy Flow in Hadronic Collisions”, *Eur.Phys.J.* **C72** (2012) 1982, doi:10.1140/epjc/s10052-012-1982-5, arXiv:1112.6354.
- [7] M. Cacciari, G. P. Salam, and G. Soyez, “The anti- $k_t$  jet clustering algorithm”, *JHEP* **04** (2008) 063, doi:10.1088/1126-6708/2008/04/063, arXiv:0802.1189.
- [8] Z. Nagy, “Three-jet cross sections in hadron hadron collisions at next-to-leading order”, *Phys. Rev. Lett.* **88** (2002) 122003, doi:10.1103/PhysRevLett.88.122003, arXiv:hep-ph/0110315.
- [9] Z. Nagy, “Next-to-leading order calculation of three jet observables in hadron hadron collision”, *Phys. Rev.* **D68** (2003) 094002, doi:10.1103/PhysRevD.68.094002, arXiv:hep-ph/0307268.
- [10] CMS Collaboration, “The CMS experiment at the CERN LHC”, *JINST* **0803** (2008) S08004.
- [11] CMS Collaboration, “Performance and Operation of the CMS Electromagnetic Calorimeter”, *JINST* **5** (2010) T03010, doi:10.1088/1748-0221/5/03/T03010, arXiv:0910.3423.
- [12] CMS Collaboration, “Performance of the CMS Hadron Calorimeter with Cosmic Ray Muons and LHC Beam Data”, *JINST* **5** (2010) T03012, doi:10.1088/1748-0221/5/03/T03012, arXiv:0911.4991.
- [13] G. Bayatian et al., “Design, performance and calibration of the CMS forward calorimeter wedges”, *Eur. Phys. J.* **C53** (2008) 139–166, doi:10.1140/epjc/s10052-007-0459-4.
- [14] M. Cacciari, G. P. Salam, and G. Soyez, “The anti- $k_t$  jet clustering algorithm”, *JHEP* **04** (2008) 063, doi:10.1088/1126-6708/2008/04/063, arXiv:0802.1189.
- [15] CMS Collaboration, “Particle-Flow Event Reconstruction in CMS and Performance for Jets, Taus and MET”, *CMS Physics Analysis Summary CMS-PAS-PFT-09-001* (2009).



- [16] CMS Collaboration, “Determination of Jet Energy Calibration and Transverse Momentum Resolution in CMS”, [arXiv:1107.4277](#).
- [17] CMS Collaboration, “Determination of the jet energy scale in CMS with pp collisions at  $\sqrt{s} = 7$  TeV”, *CMS Physics Analysis Summary* **JME-10-010** (2010).
- [18] G. D’Agostini, “A Multidimensional unfolding method based on Bayes’ theorem.”, *Nucl.Instrum.Meth.* **A362** (1995) 487.
- [19] T. Adye, “Unfolding algorithms and tests using RooUnfold”, [arXiv:physics.data-an/1105.1160](#).
- [20] CMS Collaboration, “Determination of Jet Energy Calibration and Transverse Momentum Resolution in CMS”, *JINST* **6** (2011) P11002, [doi:10.1088/1748-0221/6/11/P11002](#).
- [21] T. Sjostrand, S. Mrenna, and P. Skands, “PYTHIA 6.4 Physics and Manual”, *JHEP* **05** (2006) 026, [arXiv:hep-ph/0603175](#).
- [22] M. Bähr et al., “Herwig++ Physics and Manual”, *Eur. Phys. J.* **C58** (2008) 639, [doi:10.1140/epjc/s10052-008-0798-9](#).
- [23] CMS Collaboration, “Measurement of the inclusive production cross sections for forward jets and for dijet events with one forward and one central jet in  $pp$  collisions at  $\sqrt{s} = 7$  TeV”, *JHEP* **1206** (2012) 036, [doi:10.1007/JHEP06\(2012\)036](#), [arXiv:1202.0704](#).
- [24] CMS Collaboration, “Measurements of differential jet cross sections in proton-proton collisions at  $\sqrt{s} = 7$  TeV with the CMS detector”, [arXiv:1212.6660](#).
- [25] CMS Collaboration, “Measurements of differential jet cross sections in at  $\sqrt{s} = 8$  TeV with the CMS detector”, *CMS Physics Analysis Summary* **CMS-PAS-SMP-12-012** (2012).
- [26] P. Nason and B. Webber, “Next-to-Leading-Order Event Generators”, *Ann.Rev.Nucl.Part.Sci.* **62** (2012) 187–213, [doi:10.1146/annurev-nucl-102711-094928](#), [arXiv:1202.1251](#).
- [27] S. Alioli et al., “Jet pair production in POWHEG”, [arXiv:1012.3380](#).
- [28] Z. Nagy, “Next-to-leading order calculation of three jet observables in hadron-hadron collision”, *Phys. Rev.* **D68** (2003) 094002, [doi:10.1103/PhysRevD.68.094002](#).
- [29] T. Kluge, K. Rabbertz, and M. Wobisch, “fastNLO: Fast pQCD calculations for PDF fits”, [arXiv:hep-ph/0609285v2](#).
- [30] H.-L. Lai et al., “New parton distributions for collider physics”, *Phys. Rev.* **D82** (2010) 074024, [doi:10.1103/PhysRevD.82.074024](#).
- [31] A. D. Martin et al., “Parton distributions for the LHC”, *Eur. Phys. J.* **C63** (2009) 189, [doi:10.1140/epjc/s10052-009-1072-5](#).
- [32] R. D. Ball et al., “A first unbiased global NLO determination of parton distributions and their uncertainties”, *Nucl. Phys.* **B838** (2010) 136, [doi:10.1016/j.nuclphysb.2010.05.008](#).

- 
- [33] H1 and ZEUS Collaboration, “Combined Measurement and QCD Analysis of the Inclusive ep Scattering Cross Sections at HERA”, *JHEP* **01** (2010) 109, doi:10.1007/JHEP01(2010)109.
  - [34] S. M. S. Alekhin, J. Blümlein, “Parton distribution functions and benchmark cross sections at NNLO”, arXiv:hep-ph/1202.2281v2.
  - [35] S. Dooling, P. Gunnellini, F. Hautmann, and H. Jung, “Longitudinal momentum shifts, showering and nonperturbative corrections in matched NLO-shower event generators”, arXiv:1212.6164.